J. Fluid Mech. (2024), *vol*. 998, A48, doi:10.1017/jfm.2024.598

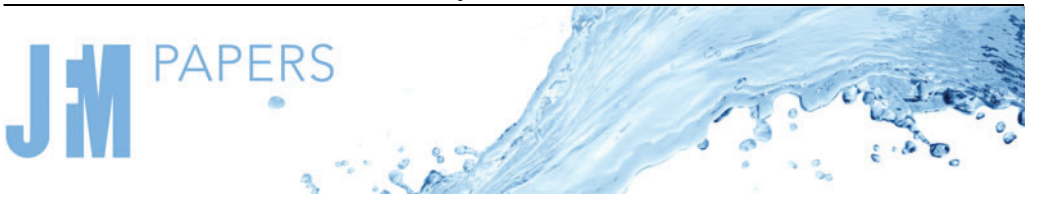

Turbulent mixed convection in vertical and horizontal channels

Christopher J. Howland[1],†, **Guru Sreevanshu Yerragolam**[1], **Roberto Verzicco**[1,2,3] **and Detlef Lohse**[1,4]

[1]Physics of Fluids Group, Max Planck Center for Complex Fluid Dynamics, and J.M. Burgers Centre for Fluid Dynamics, University of Twente, P.O. Box 217, 7500AE Enschede, The Netherlands

[2]Dipartimento di Ingegneria Industriale, University of Rome 'Tor Vergata', 00133 Roma, Italy

[3]Gran Sasso Science Institute, Viale F. Crispi, 7 67100 L'Aquila, Italy

[4]Max Planck Institute for Dynamics and Self-Organization, 37077 Göttingen, Germany

(Received 12 March 2024; revised 28 June 2024; accepted 2 August 2024)

Turbulent shear flows driven by a combination of a pressure gradient and buoyancy forcing are investigated using direct numerical simulations. Specifically, we consider the set-up of a differentially heated vertical channel subject to a Poiseuille-like horizontal pressure gradient. We explore the response of the system to its three control parameters: the Grashof number Gr, the Prandtl number Pr, and the Reynolds number Re of the pressure-driven flow. From these input parameters, the relative strength of buoyancy driving to the pressure gradient can be quantified by the Richardson number $Ri = Gr/Re^2$. We compare the response of the mixed vertical convection configuration to that of mixed Rayleigh–Bénard convection, and find a nearly identical behaviour, including an increase in wall friction at higher Gr, and a drop in the heat flux relative to natural convection for $Ri = O(1)$. This closely matched response is despite vastly different flow structures in the systems. No large-scale organisation is visible in visualisations of mixed vertical convection – an observation that is confirmed quantitatively by spectral analysis. This analysis, combined with a statistical description of the wall heat flux, highlights how moderate shear suppresses the growth of small-scale plumes and reduces the likelihood of extreme events in the local wall heat flux. *Vice versa*, starting from a pure shear flow, the addition of thermal driving enhances the drag due to the emission of thermal plumes.

Key words: turbulent convection, turbulent boundary layers, buoyant boundary layers

† Present address: School of Mathematics and Statistics, University College Dublin, Belfield, Dublin 4, Ireland. Email address for correspondence: c.j.howland@outlook.com

1. Introduction

The transport of heat by turbulent convection is integral to a wide range of natural and engineering applications, from building ventilation to the atmospheric boundary layer and the near-surface ocean. All of these examples can, under the right conditions, be classified as mixed convection. Mixed convection describes the scenario where both buoyancy and shear forces are relevant to the dynamics. This is in contrast to natural convection, where a flow is driven solely by density differences within the fluid, and forced convection, where buoyancy is negligible and the transport of heat is identical to that of a passive scalar. The relative importance of buoyancy compared to the imposed shear is quantified by the Richardson number Ri, with the extreme cases $Ri = \infty$ for purely thermal driving and $Ri = 0$ for purely shear or pressure driving.

The foundational work on mixed convection by Obukhov (1946) was motivated by understanding the dynamics of the surface layer of the atmosphere. Obukhov supposed that the dynamics was determined solely by the surface friction (quantified by the friction velocity u_τ), the surface heat flux q, and gravity g, such that dimensional analysis revealed a single possible length scale $L_O = u_\tau^3/g\alpha q$ that could describe the system. Using this length to rescale the problem, Monin & Obukhov (1954) derived what is now known as the Monin–Obukhov similarity theory (MOST), where 'universal' functions of z/L_O are used to describe the mean velocity and temperature profiles in stably or unstably stratified shear flows. These universal functions are obtained by interpolating between the extreme cases of natural convection and forced convection, which were updated by Kader & Yaglom (1990) for unstable (i.e. convecting) boundary layers. A historical overview of MOST is provided in Foken (2006), and the theory has been extremely popular in atmospheric and oceanic applications. However, some of the assumptions underlying MOST have recently been coming under further scrutiny, particularly the power-law dependence of the mean profiles in the convective regime (Cheng *et al.* 2021).

Mixed convection has also often been studied in simple, canonical flow configurations where the system response is dependent only on a small number of dimensionless input parameters. A popular approach has been to introduce horizontal forcing into the classical Rayleigh–Bénard (RB) set-up, either through a horizontal pressure gradient (Poiseuille–Rayleigh–Bénard, P-RB) or by setting one of the boundary plates in motion (Couette–Rayleigh–Bénard, C-RB). The linear stability of the P-RB system was studied by Gage & Reid (1968), who found that streamwise perturbations are suppressed by the introduction of shear, so the fastest growing mode takes the form of convective rolls in the plane orthogonal to the mean flow. Note that the critical Rayleigh number $Ra_c = 1708$ and the fastest growing wavelength $\lambda = 2\sqrt{2}H$ do not change compared to natural RB since the linear problem is unchanged in the orthogonal plane. Such streamwise-aligned rolls were observed experimentally by Richter & Parsons (1975) in C-RB, although since their set-up was motivated by mantle convection, their working fluid had a very high Prandtl number $Pr = 8600$ and low Reynolds numbers. Domaradzki & Metcalfe (1988) performed simulations of C-RB, also finding organisation into streamwise-aligned rolls but at the largest wavelength of the domain. More recent direct numerical simulations in larger domains by Pirozzoli *et al.* (2017) for P-RB and Blass *et al.* (2020, 2021) for C-RB highlight how these large-scale structures contribute a large proportion of the heat and momentum flux in mixed RB, and how their wavelength depends on the Richardson number Ri of the system. Madhusudanan *et al.* (2022) recently reproduced the wide rolls using a linear model coupled to eddy diffusivities, showing that they are generated primarily through a classical lift-up mechanism.

The response of canonical mixed convection systems can be quantified using the friction coefficient C_f and the Nusselt number Nu, which measure the dimensionless skin friction and heat flux. In forced convection, where buoyancy is negligible, both Poiseuille and Couette flows exhibit an identical response in C_f when appropriately scaled using the centreline velocity (Orlandi, Bernardini & Pirozzoli 2015). Scagliarini *et al.* (2015) observed an increase in the streamwise friction coefficient in P-RB relative to pure Poiseuille flow, for which they proposed a modified formulation of the log law for the mean velocity in the presence of convection. An intriguing phenomenon of mixed RB is found in the response of the heat flux, which varies non-monotonically with Reynolds number Re for fixed Rayleigh number and Prandtl number. Nusselt number Nu first decreases relative to the natural convection case, before increasing at high Re as the flow enters the forced convection regime (Blass *et al.* 2020, 2021). This behaviour, not predicted by MOST, has been attributed to the sweeping away of thermal plumes by the imposed horizontal flow. The plume sweeping concept has since been applied to form phenomenological models of the system (Scagliarini, Gylfason & Toschi 2014). Similar to the response of the friction coefficient, an identical response is found in P-RB and C-RB when appropriately scaled, and the decrease in Nu has recently been shown to collapse onto a single curve when the Reynolds number of the shear flow is considered relative to the Reynolds number of the natural convection (Yerragolam *et al.* 2024). Yerragolam *et al.* (2024) also provide a theoretical estimate for this decrease in heat flux based on an extension of the Grossmann & Lohse (2000, 2001) theory for RB convection to mixed RB.

The interplay of shear and convection has an important role in another canonical natural convection problem: the differentially heated vertical channel, often simply referred to as vertical convection (VC). In this configuration, convection drives flow parallel to the boundary plates, generating a mean shear at the walls and in the bulk of the channel. An analogy can be drawn between the large-scale circulation in RB and the vertical mean flow in VC, but since the vertical buoyancy flux is not equivalent to the heat flux of interest in VC, the Grossmann & Lohse (2000) approach of linking heat flux and kinetic energy dissipation cannot be applied directly. Nevertheless, Ng *et al.* (2015) found similar scaling relations to RB for heat flux and dissipation rates in VC when conditionally sampling either the boundary layers or the bulk. Recent simulations at varying Prandtl number (Howland *et al.* 2022) have prompted renewed efforts to understand the boundary layer theory limiting the global response of the system (Ching 2023) and the dynamics setting the mean profiles in the channel centre (Li *et al.* 2023).

Mixed convection in a vertical channel, where an additional pressure-driven forcing is applied to the VC configuration, has been less well studied than mixed RB. The majority of studies into these flows (e.g. Kasagi & Nishimura 1997; Wetzel & Wagner 2019; Guo & Prasser 2022) impose a mean pressure gradient in the vertical direction that directly opposes or enhances the mean flow due to convection. Although this configuration is relevant to some industrial applications, from a physical perspective it breaks the symmetry of the channel, with the boundary layers at each wall subject to different shear stresses. In this study, we instead impose a horizontal pressure gradient in the channel, which leads to symmetric profiles of horizontal velocity and higher-order statistics while retaining the anti-symmetric profiles of mean vertical velocity and temperature from VC. Although we approach this configuration from a fundamental point of view, the crossflow set-up can be relevant to industrial heat exchangers in a wide range of applications. We are aware of only one other paper discussing such a system (El-Samni, Yoon & Chun 2005), which highlights tilted structures at the wall and a modification of the near-wall Reynolds stresses. However, the results of El-Samni *et al.* (2005) are mainly descriptive and cover a limited parameter range.

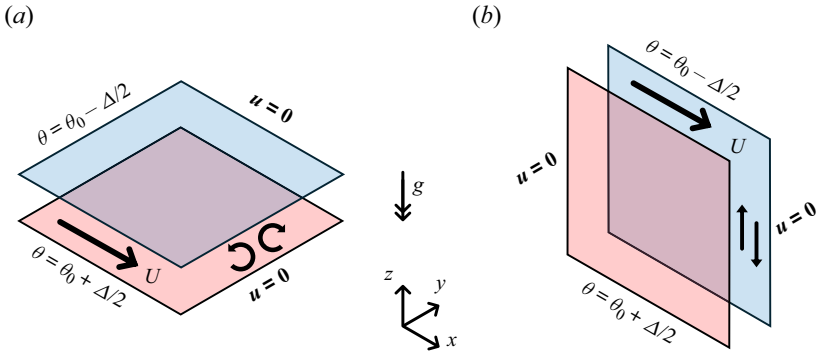

Figure 1. Schematics of canonical mixed convection systems. (*a*) Mixed RB convection with Poiseuille-type forcing as studied by e.g. Domaradzki & Metcalfe (1988), Pirozzoli *et al.* (2017) and Yerragolam *et al.* (2024). (*b*) Mixed VC with Poiseuille-type forcing, as used for the new simulations presented in this paper. Large arrows highlight the imposed horizontal pressure gradient, and smaller arrows highlight the large-scale flows driven by buoyancy in each configuration. The acceleration due to gravity is highlighted by a double arrow.

In the current paper, we use direct numerical simulations to explore the dynamics of turbulent mixed convection in a vertical channel for a wide range of parameters, focusing on the transition between natural convection and forced convection. The paper is organised as follows. First, in § 2, we describe the problem set-up and details of the numerical simulations, before presenting visualisations of the resulting flow in § 3. The global response of the system is investigated in terms of the friction coefficients and the Nusselt number, and compared with the mixed RB flow in § 4. We then turn to wall-normal profiles in mixed VC in § 5, focusing primarily on the balances in the mean momentum budgets. Detailed analysis of the heat transport is then performed by spectral analysis in § 6, and through statistics of the boundary layers in § 7. Finally, our conclusions are presented in § 8, where we discuss the implications of our results and provide an outlook on future research in mixed convection.

2. Simulation set-up and numerical methods

We perform numerical simulations of the flow arising in a fluid confined between two parallel no-slip vertical walls. The walls are separated by a horizontal distance H and are held at fixed temperatures, with a temperature difference Δ between the plates. As in the schematic in figure 1(*b*), we take the x-coordinate to be horizontal and parallel to the plates, the y-coordinate to be normal to the boundaries, and z to be in the vertical direction. We consider a fluid satisfying the Oberbeck–Boussinesq approximation, such that changes in density are significant only in the buoyancy term, and are linear with respect to changes in temperature. We therefore treat the velocity field $\boldsymbol{u} = (u, v, w)$ as divergence-free ($\boldsymbol{\nabla} \cdot \boldsymbol{u} = 0$) and satisfying the Navier–Stokes momentum equation

$$\partial_t \boldsymbol{u} + (\boldsymbol{u} \cdot \boldsymbol{\nabla})\boldsymbol{u} = -\rho^{-1}\,\boldsymbol{\nabla} p + \nu\,\nabla^2 \boldsymbol{u} + g\alpha\theta\hat{\boldsymbol{z}} + G\hat{\boldsymbol{x}}, \tag{2.1}$$

where ρ is the mean fluid density (assumed constant), p is the pressure, ν is the kinematic viscosity, g is the acceleration due to gravity, and α is the thermal expansion coefficient. A time-dependent, spatially uniform forcing $G(t)$ is applied in the streamwise (x) direction to maintain a constant mean flow $\langle u \rangle = U$. The magnitude of this forcing is computed at every time step to exactly cancel out any variation in the mean flow. Previous work has

shown that such a forcing produces results near-identical to those of a constant pressure gradient (Quadrio, Frohnapfel & Hasegawa 2016), but allows us to use the mean flow strength as an input parameter. The temperature field θ satisfies the advection–diffusion equation

$$\partial_t \theta + (\boldsymbol{u} \cdot \boldsymbol{\nabla})\theta = \kappa \, \nabla^2 \theta, \tag{2.2}$$

where κ is the thermal diffusivity. Periodic boundary conditions are applied to both $\boldsymbol{u}$ and θ in the x and z directions. Unless otherwise stated, the aspect ratio of the domain in these periodic directions is taken as $\Gamma = L/H = 8$, such that the length of the domain L in x and z is equal, and eight times the plate separation distance H.

We perform direct numerical simulations of (2.1) and (2.2) using a highly parallelised flow solver that computes spatial derivatives using second-order central finite differences on a staggered grid configuration. The wall-normal diffusive terms are evolved in time using a Crank–Nicolson scheme, and all other terms are treated explicitly using a three-stage Runge–Kutta method. An adaptive time step is chosen using the constraint of a maximum Courant number of 1. The velocity is kept divergence-free to machine precision using a pressure correction step at each time step that is implemented with fast Fourier transforms in the periodic directions and a tridiagonal matrix solver in the wall-normal direction. A multiple-resolution technique is applied to evolve the velocity and temperature fields on independent grids, with cubic Hermite interpolation used for the buoyancy forcing and the advection of temperature. Detailed overviews of the numerical discretisation, the domain decomposition strategy and the multiple-resolution technique can be found in Verzicco & Orlandi (1996), van der Poel *et al.* (2015) and Ostilla-Monico *et al.* (2015), as well as in our software documentation.

The physical input parameters of the system are the Rayleigh number, the Prandtl number and the Reynolds number:

$$Ra = \frac{g\alpha \, \Delta H^3}{\nu\kappa}, \quad Pr = \frac{\nu}{\kappa}, \quad Re = \frac{UH}{\nu}. \tag{2.3a–c}$$

When considering the strength of the flow driven by convection, it is often useful to consider the Grashof number Gr as the relevant input parameter, and when comparing the relative strengths of buoyancy to pressure driving, we can construct a Richardson number as

$$Gr = \frac{Ra}{Pr} = \frac{g\alpha \, \Delta H^3}{\nu^2} = \left(\frac{U_f H}{\nu}\right)^2, \quad Ri = \frac{Gr}{Re^2} = \frac{g\alpha \, \Delta H}{U^2} = \left(\frac{U_f}{U}\right)^2. \tag{2.4a,b}$$

These can both be considered as input parameters. Above, we have written $U_f = \sqrt{g\alpha \, \Delta H}$ as the free-fall velocity scale to give insight into the interpretation of these parameters.

In this study, we perform two sets of simulations to compare the relative impacts of the various input parameters. First, we fix $Gr = 10^6$ and vary $1 \leq Pr \leq 10$ along with $10^{2.5} \leq Re \leq 10^4$, which correspond to Richardson numbers $10^{-2} \leq Ri \leq 10$. For the second set, we fix $Pr = 1$ and increase Gr up to 10^8 while again varying Re up to 10^4. A detailed overview of the parameters used for each simulation is given in table 1 of Appendix B. Each simulation is run to a statistically steady state, in which the flow statistics are computed and averaged for a minimum of 200 advective time units. For high $Ri \geq 1$, the relevant time unit is H/U_f, whereas for low $Ri \leq 1$, the relevant time unit is H/U. The wall-normal grid spacing is stretched following Pirozzoli & Orlandi (2021) to ensure sufficient resolution close to the wall, such that $\Delta y^+ < 0.1$ at the wall

for the base velocity grid. In the periodic directions, the uniform grid spacing satisfies $\Delta x^+ \leq 5.4$ in every simulation. At the centre of the domain, the spacing of the refined grid satisfies $\Delta y_r \leq 1.05 l_B$, $\Delta x_r < 1.4 l_B$, where l_B is the Batchelor scale computed using the plane-averaged turbulent kinetic energy (TKE) dissipation rate over the midplane. Full details of the grid sizes are provided in Appendix B.

3. Flow visualisation

We begin with a qualitative comparison of the simulations through visualisations of the temperature field and the local heat flux. Figure 2 displays the instantaneous local wall-normal heat flux at the boundary plate $y = 0$ for cases with fixed $Pr = 1$, and ranges $10^6 \leq Gr \leq 10^8$, $10^3 \leq Re \leq 10^4$. The dimensionless heat flux plotted here is defined as

$$q_\theta(x, z, t) = -\frac{H}{\Delta} \left. \frac{\partial \theta}{\partial y} \right|_{y=0}, \tag{3.1}$$

such that its time- and plane-averaged value is equivalent to the Nusselt number, $Nu = \overline{q_\theta}$.

As mentioned above, the relative strength of convection to the horizontal flow can be characterised by the Richardson number $Ri = Gr/Re^2$, which is constant along diagonals in figure 2. At high Ri, as in figure 2(c), the horizontal flow has little impact on the local distribution of the wall heat flux. The near-wall temperature structures are the same as in the case of no crossflow, with regions of large local heat flux (dark spots) separated by longer, streaky structures aligned in the vertical (Howland *et al.* 2022). As Ri decreases, such as in figures 2(e,i) where $Ri = 1$, the prominence of the large heat flux regions diminishes, and the streaks become aligned in the diagonal. This visualises the local direction of the flow along the wall, which at $Ri = 1$ is due to a combination of the VC and the horizontal pressure gradient. At lower Ri, these structures become more aligned with the horizontal, eventually spanning the domain as in figure 2(g), which is reminiscent of classical low-speed streaks in turbulent channel flow (Kline *et al.* 1967; Antonia, Abe & Kawamura 2009). A more quantitative analysis of the change in the near-wall heat flux distribution will be provided in § 7.

In figure 3, we present visualisations of the same simulations but now at the midplane of the simulation domain $y = H/2$. As would be expected, the fields at higher Gr and Re exhibit structures with a wider range of spatial scales. Aside from this dynamical range, the effect of increasing Re is less noticeable at the midplane than at the wall in figure 2. At the centre of a turbulent channel, the mean profile of horizontal velocity is relatively flat, with zero mean shear and a local minimum in TKE. By contrast in VC, a mean shear in the vertical velocity drives the generation of turbulence in the bulk, argued by Li *et al.* (2023) to follow a mixing-layer-like behaviour. In figure 3, greater mixing at higher Gr leads to smaller values of the temperature perturbations in the midplane, although the same effect is not evident as Re increases. Compared to the mixed RB system, where gravity is orthogonal to the plates and the temperature field organises into large, streamwise-aligned coherent rolls, the fields in mixed VC appear rather featureless. A hint of such large-scale rolls is noticeable only for the cases dominated by strong pressure driving with high Re and low Ri (figures 3g,h), where the temperature structures appear more aligned along the streamwise (x) axis. This contrast in the organisation of mixed convection systems will be investigated more quantitatively in § 6 through spectral analysis, but we first turn to the global responses of the two mixed convection systems in the next section.

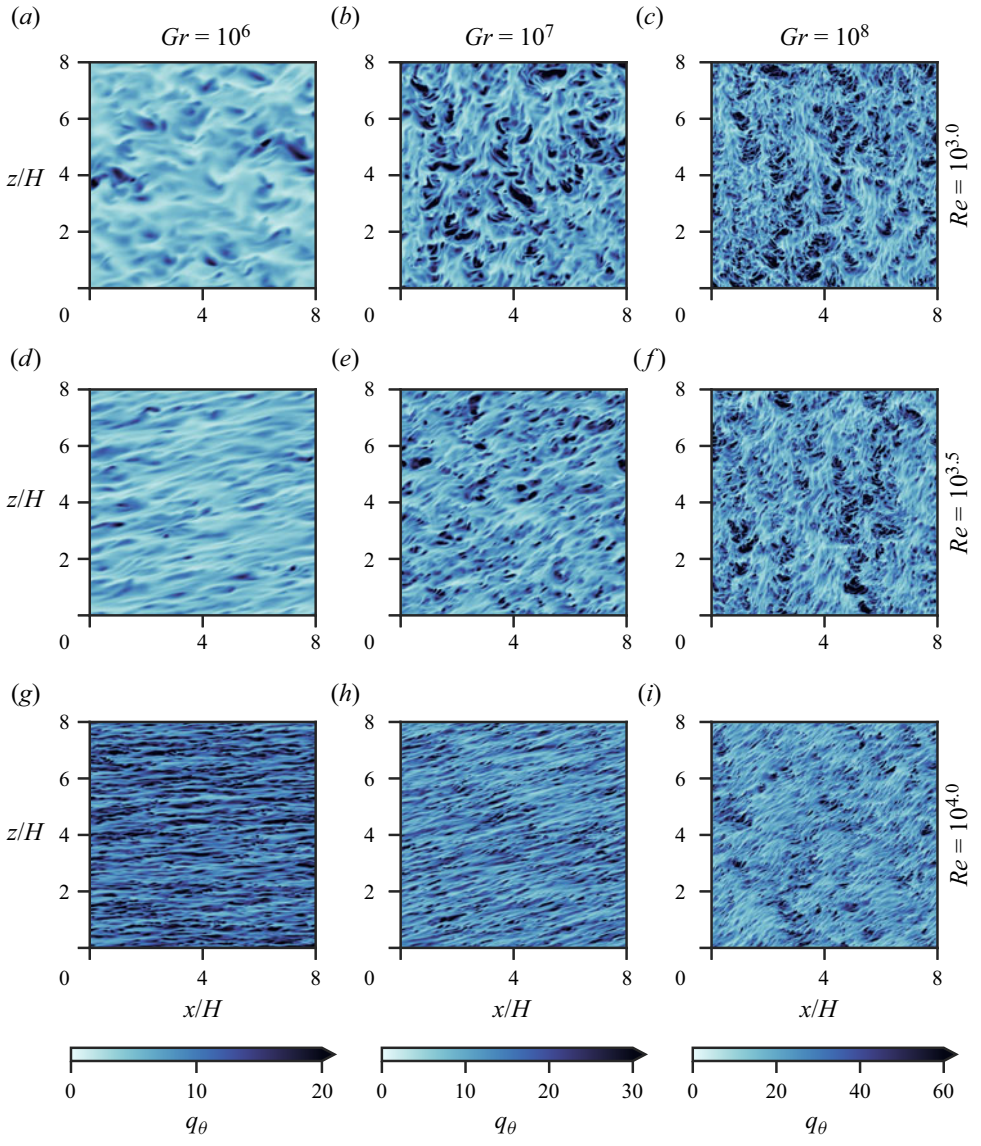

Figure 2. Vertical planes of the instantaneous local wall-normal heat flux at the boundary $y = 0$. All simulations shown are with fixed $Pr = 1$. The Richardson number $Ri = Gr/Re^2$ is comparable along diagonals from the upper left to the lower right, with the largest value ($Ri = 100$) in the top right and the lowest value ($Ri = 0.01$) in the bottom left. This figure is also available as an interactive JFM notebook: https://www.cambridge.org/S0022112024005986/JFM-Notebooks/files/Figure-2.ipynb.

4. Global response quantities in mixed convection systems

In this section, we compare the responses of the mixed VC set-up with those of mixed RB using the simulation data of Yerragolam *et al.* (2024). Those simulations cover comparable ranges of parameters $10^6 \leq Gr \leq 10^8$, $0.5 \leq Pr \leq 5$ and $Re \leq 10^4$ in a domain of streamwise aspect ratio $\Gamma_x = 8$ and spanwise aspect ratio $\Gamma_y = 4$. The flow solver shares an identical code base except for the multiple-resolution technique, which is used only in the newly reported mixed VC simulations.

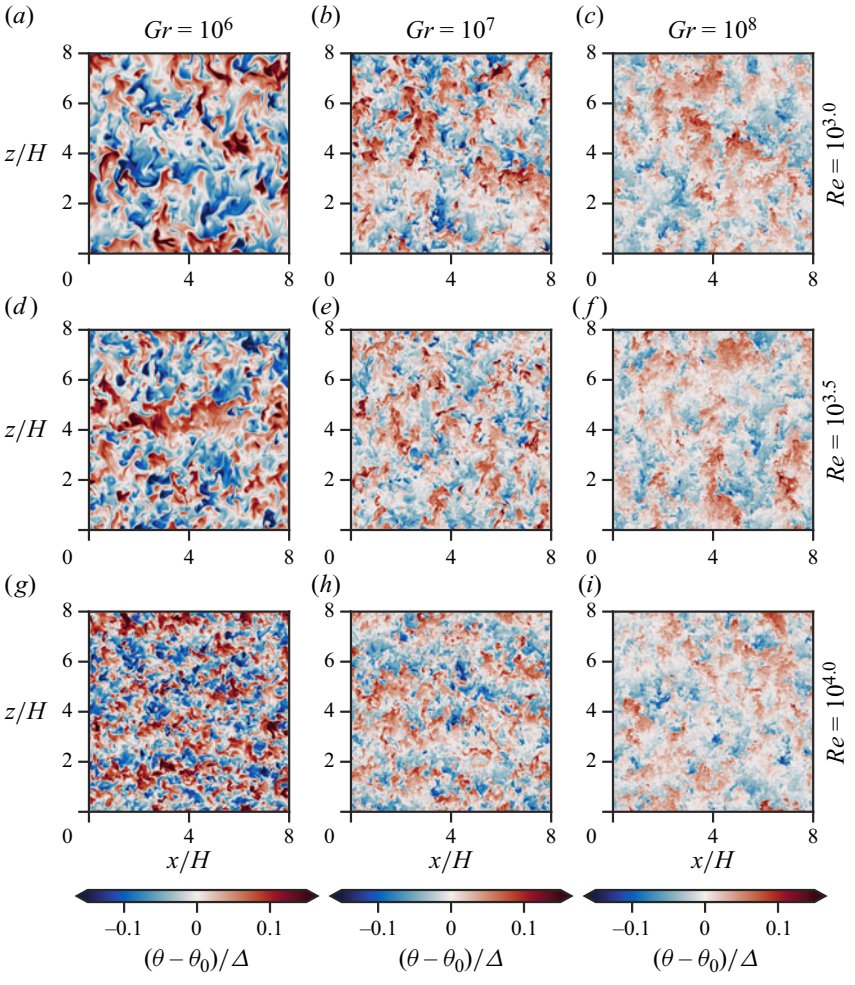

Figure 3. Vertical planes of the temperature field at the channel centre $y = H/2$. See the caption of figure 2 for details of the simulations presented. Here, θ_0 is the arbitrary reference temperature that is the midpoint of the two boundary values. This figure is also available as an interactive JFM notebook: https://www.cambridge.org/S0022112024005986/JFM-Notebooks/files/Figure-3.ipynb.

4.1. *Friction coefficients*

A key global response parameter in shear-driven flows is the friction coefficient

$$C_f = \frac{2\tau}{\rho U^2}, \tag{4.1}$$

where τ is the wall shear stress and U is the velocity magnitude in the bulk. Since the friction coefficient is determined solely by the velocity field, we expect the dependence on the Prandtl number to be relatively weak, and consider a relationship $C_f(Re)$. Power-law scalings for $C_f(Re)$ can be derived for laminar boundary layer flows, with e.g. $C_f \sim Re^{-1}$ applicable to Couette or Poiseuille flows, and $C_f \sim Re^{-1/2}$ arising from the classical Blasius boundary layer solution (Schlichting & Gersten 2016). For a turbulent boundary

layer in the sense of Prandtl and von Kármán, the friction coefficient satisfies the relation

$$\sqrt{\frac{2}{C_f}} = \frac{1}{\kappa_u} \log\left(Re\sqrt{\frac{C_f}{8}}\right) + B, \tag{4.2}$$

known as the Prandtl friction law after Prandtl (1932). The von Kármán constant κ_u typically takes a value of approximately 0.4, and the intercept B is close to 4, but the exact values, their universality and the way in which they are fit to data remain an active topic of research (Monkewitz & Nagib 2023). Due to our similar set-up and numerical methods, we take the values suggested by Pirozzoli, Bernardini & Orlandi (2014), namely $\kappa_u = 0.41$ and $B = 5$.

Since the mixed VC flow is driven in orthogonal directions by the pressure gradient and by buoyancy, we can construct separate friction coefficients for each component of the wall shear stress. Understanding the response of the friction coefficients in this context relies on choosing an appropriate Reynolds number for each component of the flow. For the streamwise (x) direction in which the mean flow is imposed by a pressure gradient, this Reynolds number is simply the input parameter defined in (2.3*a–c*).

We consider the response of the streamwise friction coefficient in figure 4, where only the streamwise component of the shear stress $\tau = \rho\nu\,\partial_y\bar{u}$ is applied to the definition (4.1). The global response of mixed VC is near identical to that of mixed RB, with a transition from a laminar power-law scaling to the Prandtl friction law of (4.2). For comparable parameter values, the largest difference in C_f between the mixed RB and mixed VC cases is 16 %. In the laminar scaling regime, stronger buoyancy driving (characterised by higher Gr) leads to an increase in the streamwise skin friction for a given Re. As suggested earlier, the dependence of C_f on Pr is very weak compared to the other control parameters. Unlike in standard Poiseuille or Couette flow, where a subcritical transition arises due to instability of the laminar base flow and leads to a jump in C_f, the streamwise boundary layer transition in mixed convection systems appears smooth. We anticipate that the laminar scaling regime remains relevant until its intersection with the friction law (4.2). The increase of C_f with Gr in the laminar regime would therefore delay the transition to this 'fully turbulent' Prandtl friction law (4.2) to higher Re. At low Re, although the relationship exhibits a laminar-like scaling, one should recall that the convection flow in the interior remains turbulent. In figure 4(*b*), we focus on clarifying this low Re regime and the increase in C_f with stronger convection. Across both mixed convection systems and for a range of Pr, we find a collapse of the data upon rescaling by $Gr^{1/4}$. The Re^{-1} scaling that arises from laminar profiles in Couette/Poiseuille flow appears somewhat too steep to describe the data accurately. Blass *et al.* (2020) reported a scaling $C_f \sim Re^{-0.90}$ in C-RB, but at this time there is no theoretical basis for such a scaling. Note that one could equivalently express the simplified Re^{-1} collapse as $C_f \sim Ri^{1/4}\,Re^{-1/2}$ using the definitions of (2.3*a–c*). In the case of mixed convection, the buoyancy-driven flow generates non-zero Reynolds stresses in the equation for the mean profile, which can be expected to modify the mean momentum budget and lead to such an increase in C_f. This will be analysed in further detail for mixed VC in § 5.

We now turn to the friction coefficient associated with the buoyancy-driven component of the flow. For the mixed VC system, we can simply take the peak velocity W_{max} of the mean vertical velocity $\bar{w}(y)$ as the relevant velocity scale, and directly measure the mean vertical shear stress at the wall, $\tau = \rho\nu\,\partial_y\bar{w}$. In the RB configuration, the convection has no preferential direction along the walls, resulting in zero mean shear stress. However, we can still construct a friction coefficient associated with the persistent large-scale circulation

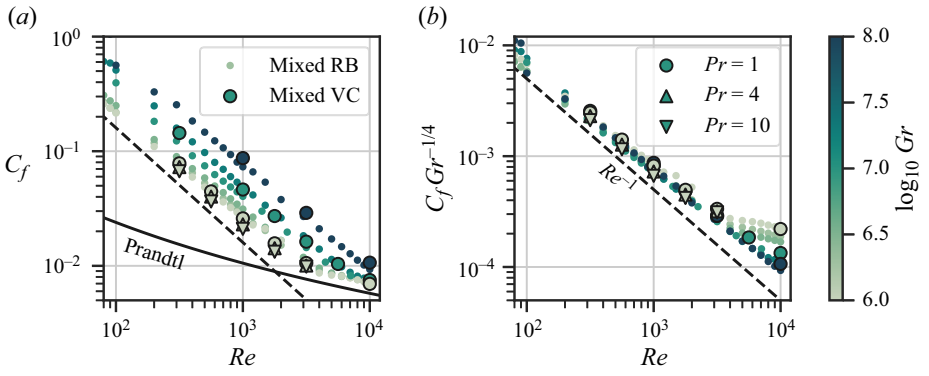

Figure 4. (*a*) Friction coefficients calculated for the streamwise component of velocity as a function of Reynolds number. (*b*) Friction coefficients normalised by $Gr^{1/4}$ to collapse the data at low Re. Large markers are used for the mixed VC simulations, whereas small dots show the data from the mixed RB cases of Yerragolam *et al.* (2024). Grashof numbers are highlighted by the colour of the markers, and for the mixed VC cases, different markers signify different Pr. Black dashed lines show a scaling law of Re^{-1}, and the black solid line marks the Prandtl friction law of (4.2). This figure is also available as an interactive JFM notebook: https://www.cambridge.org/S0022112024005986/JFM-Notebooks/files/Figure-4.ipynb.

by using the root mean square (r.m.s.) horizontal velocity profile $u_H(y) = (\overline{u^2 + v^2})^{1/2}$. When a horizontal crossflow is added to the RB system, the large-scale circulation aligns itself perpendicular to the imposed flow (Pirozzoli *et al.* 2017; Yerragolam *et al.* 2022), so for the mixed RB cases, we construct a friction coefficient using only the spanwise r.m.s. velocity. Defining the friction coefficient in this way will be appropriate only for cases where the convectively driven flow is stronger than the spanwise velocity fluctuations induced by the turbulent shear flow, i.e. for $Ri \geq O(1)$.

In terms of the Reynolds number, the plate separation H is no longer the appropriate length scale for describing the boundary layer dynamics of the convectively driven flow. As shown in the inset of figure 5(*a*), the mean profile $\bar{w}(y)$ of the vertical velocity in (mixed) VC reaches its peak value at a certain wall-normal distance δ. From this, we can define a boundary layer Reynolds number

$$Re_\delta = \frac{W_{max}\delta}{\nu} \tag{4.3}$$

that drives the behaviour at the wall. We construct an analogous Reynolds number for the mixed RB system using the spanwise r.m.s. velocity profile. The friction coefficients of the convective flow component are plotted against Re_δ in figure 5. Note that Re_δ is not known *a priori*, but is itself a response parameter of the system that varies with Gr, Pr and Re. Similar to the low-Re regime for the streamwise friction, we observe a power-law scaling close to $C_f \sim Re_\delta^{-1}$.

This is made clearer in figure 5(*b*), where we collapse the data using the friction coefficient C_0 and Reynolds number $Re_{\delta,0}$ obtained from the corresponding natural convection flows, matching Ra and Pr. Deviations from the scaling relation are observed for cases where $Ri < 1/4$, highlighted by translucent symbols in the figure. As mentioned above, for the mixed RB system this is likely an artefact of using the spanwise r.m.s. velocity to construct the friction coefficient. However, we also observe the discrepancy for low Ri in mixed VC, suggesting that at low Richardson numbers, the turbulence generated by the imposed horizontal flow disrupts the near-wall vertical velocity. Within the range of parameters explored here, the pressure-driven horizontal flow does not modify the

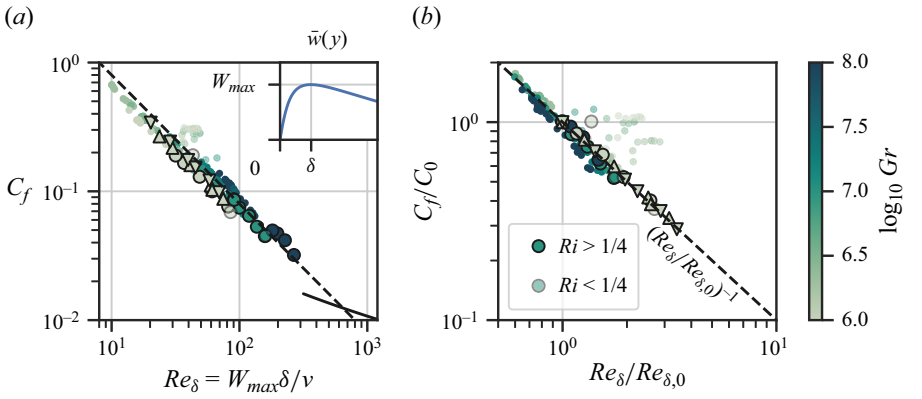

Figure 5. (*a*) Friction coefficients associated with the convectively driven flow as a function of the boundary layer Reynolds number $Re_\delta = W_{max}\delta/\nu$, where W_{max} and δ are computed as in the mean velocity profile shown in the inset. (*b*) The same data normalised against the values from the corresponding natural convection system. For the mixed VC cases, different symbols denote different Pr values as outlined in the legend of figure 4. The colour of the markers represents Gr, and simulations with $Ri < 1/4$ are plotted as semi-transparent. This figure is also available as an interactive JFM notebook: https://www.cambridge.org/S0022112024005986/JFM-Notebooks/files/Figure-5.ipynb.

vertical Re_δ by more than a factor 4, suggesting that even in the case of mixed convection, the primary control parameters determining Re_δ are Gr and Pr. As discussed in the Appendix of Howland *et al.* (2022), a 'fully turbulent' transition of this boundary layer may be possible, analogous to the so-called 'ultimate regime' in RB convection (Lohse & Shishkina 2023), but only at very high Gr. A more in-depth analysis of the mean vertical momentum budget in mixed VC will be presented in § 5.

4.2. *Nusselt number*

The dimensionless heat flux through the system is characterised by the Nusselt number, defined as

$$Nu = \frac{F_\theta}{\kappa \Delta/H}, \quad F_\theta = -\kappa \frac{\partial \bar{\theta}}{\partial y} + \overline{v'\theta'}. \tag{4.4a,b}$$

Here, F_θ is the horizontal heat flux through the system (normalised by the specific heat ρc_p), and the overbar denotes averaging in time and in directions parallel to the plates. Integration of the mean temperature equation (3.1) shows that F_θ is constant across the domain in a statistically steady state.

In figure 6(*a*), we plot the Nusselt number compensated by $Pr^{1/2}$. This prefactor seems appropriate for the Pr dependence of passive scalar transport in turbulent boundary layers when $Pr \lesssim O(1)$ (Kays *et al.* 2005), although at higher Pr, one expects a transition towards a $Pr^{1/3}$ dependence (Kader & Yaglom 1972; Alcántara-Ávila & Hoyas 2021). The data of both systems converge towards the expression

$$Nu \approx \frac{C_f(Re)}{4} Re\, Pr^{1/2}, \tag{4.5}$$

where $C_f(Re)$ follows the Prandtl law of (4.2). This expression draws a parallel between the transport of heat and momentum at the wall, known as the Reynolds analogy, and describes the heat transport in 'forced convection' when buoyancy no longer affects the flow. From these data, we anticipate that the forced convection expression (4.5) applies

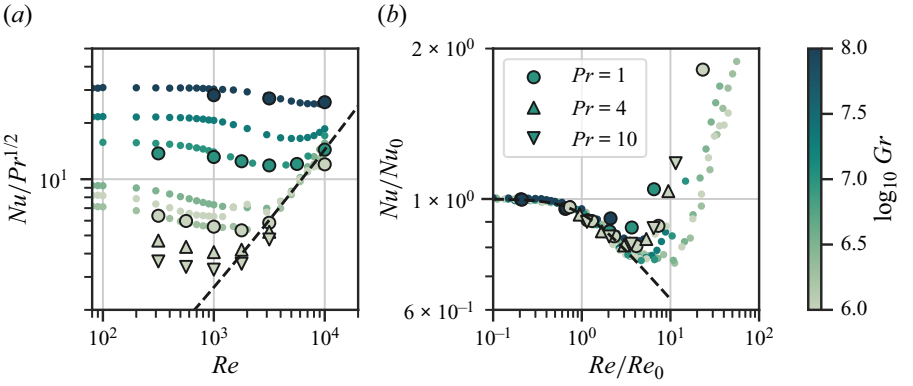

Figure 6. Nusselt numbers plotted as functions of Reynolds number. (*a*) The Nusselt number is normalised by $Pr^{1/2}$ to focus on the response in the shear-dominated regime at high Re. The black dashed line marks the Reynolds analogy $Nu \approx \frac{1}{4} C_f \, Re \, Pr^{1/2}$, where C_f satisfies the Prandtl friction law (4.2). (*b*) The data are normalised by the values associated with natural convection. Here, the black dashed line marks the recently proposed scaling relation $Nu/Nu_0 \sim (\sqrt{1 + (Re/Re_0)^2})^{-1/5}$ from Yerragolam *et al.* (2024). This figure is also available as an interactive JFM notebook: https://www.cambridge.org/S0022112024005986/JFM-Notebooks/files/Figure-6.ipynb.

for Reynolds numbers greater than that where the friction coefficient begins to follow the turbulent friction law shown in figure 4. At low Re (or more precisely high Ri), the Nusselt number responses of the two systems (VC and RB) do not match as precisely as the friction coefficients. Indeed, in the absence of an external flow, VC and RB do not exhibit the same $Nu(Ra, Pr)$ response due to the lack of coupling between the kinetic energy budget and the heat flux in VC (Ng *et al.* 2015).

However, we observe a more universal behaviour when the Nusselt numbers in the mixed convection systems are normalised by the values for the equivalent natural convection systems $Nu_0(Gr, Pr, Re) = Nu(Gr, Pr)|_{Re=0}$. In figure 6(*b*), the normalised Nusselt numbers are plotted as a function of the input Reynolds number normalised by the Reynolds number of the natural convection case $Re_0 = W_0 H/\nu$. For the mixed VC cases, we define $W_0(Gr, Pr, Re) = W_{max}(Gr, Pr)|_{Re=0}$ as the peak velocity of the natural VC flow, as highlighted in the inset of figure 5(*a*). For mixed RB, we follow Yerragolam *et al.* (2024) in using the volume-averaged r.m.s. velocity for W_0, and note that the results are insensitive to this choice of velocity scale in describing the 'wind' of the large-scale circulation. For $Re/Re_0 = O(1)$, all the data from both configurations collapse onto a single curve, showing a drop in the heat flux of up to 25 %. Given this collapse, the Re_0 of the natural convection appears to be a critical Re above which the Nusselt number is significantly affected by the horizontal crossflow. Yerragolam *et al.* (2024) provide an estimate for the drop in Nu, derived from the kinetic energy balance in mixed RB, but this balance cannot be related to the horizontal heat flux that is relevant for mixed VC.

In summary, in this section we have demonstrated the universality in the global response parameters of mixed RB and mixed VC, namely in the friction coefficient C_f and the Nusselt number, and the limitations of this universality. In the following sections, we will compare more local quantities, starting with the wall-normal profiles.

5. Wall-normal profiles in mixed VC

We now turn to the first- and second-order statistics, averaged parallel to the plates, to further investigate the dynamics behind the observed global responses. For clarity, we

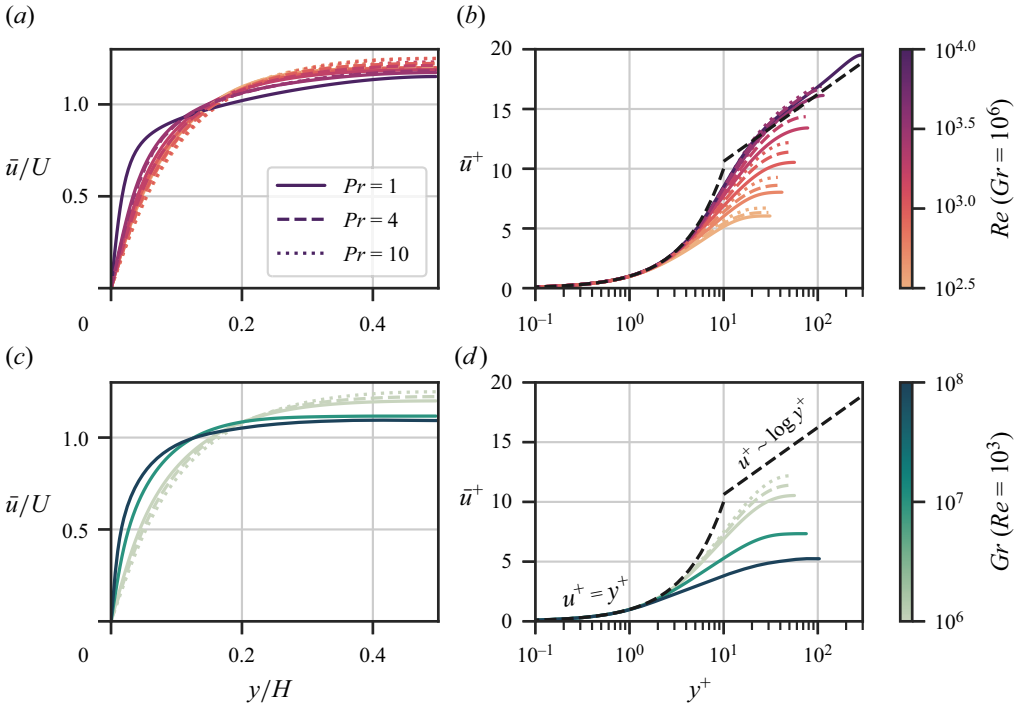

Figure 7. Mean profiles of the streamwise velocity $\bar{u}(y)$. (*a*,*b*) Data from simulations at a fixed $Gr = 10^6$, varying Re and Pr. The Re variation is denoted by the line colour, and the Pr variation is denoted by the line style. (*c*,*d*) Present data from simulations at a fixed $Re = 10^3$, varying Gr and Pr. (*a*,*c*) The profiles are normalised by the imposed bulk velocity $\langle u \rangle = U$ and the plate separation H. (*b*,*d*) The profiles are presented in viscous wall units, where $\bar{u}^+ = \bar{u}/u_\tau$ and $y^+ = yu_\tau/\nu$. Dashed black lines represent the linear relation $u^+ = y^+$ and the logarithmic region $u^+ = \kappa_u^{-1} \log y^+ + B$, where the von Kármán constant $\kappa_u = 0.41$ and $B = 5$ are taken from Pirozzoli *et al.* (2014). This figure is also available as an interactive JFM notebook: https://www.cambridge.org/S0022112024005986/JFM-Notebooks/files/Figure-7.ipynb.

focus solely on the new simulations of mixed VC, and study the variation across the three-parameter space of Gr, Pr and Re.

We begin with the response of the mean streamwise velocity $\bar{u}(y)$ in figure 7. For a fixed $Gr = 10^6$, as in figures 7(*a*,*b*), the effect of increasing Re can be seen most clearly when the mean velocity profiles are scaled by viscous wall units in figure 7(*b*). As Re increases, the velocity profile tends towards the classical log-law profile, with the case $Re = 10^4$ closely matching the profile of turbulent Poiseuille flow, as in e.g. Lee & Moser (2015). The effect of stronger thermal convection on the mean profile is also similar to that observed in other mixed convection systems in the literature (Scagliarini *et al.* 2015; Blass *et al.* 2020). In figure 7(*c*), where $Re = 10^3$ is fixed and Gr varies between 10^6 and 10^8, higher Gr leads to a flatter mean profile in the bulk of the channel. This is illustrated further in wall units in figure 7(*d*), where a significant drop in $\bar{u}^+$ is observed for $y^+ = O(10)$. Plus symbols denote scaling in viscous wall units, with velocity $u_\tau = \sqrt{\tau_u/\rho}$ and length ν/u_τ. Such a drop is consistent with the previous findings of Scagliarini *et al.* (2015) for mixed RB, who proposed a modified log law based on mixing length arguments coupled to the temperature field.

Further insight for the streamwise velocity can be gained from the appropriate component of the Reynolds stress. Considering a statistically steady state, we average the

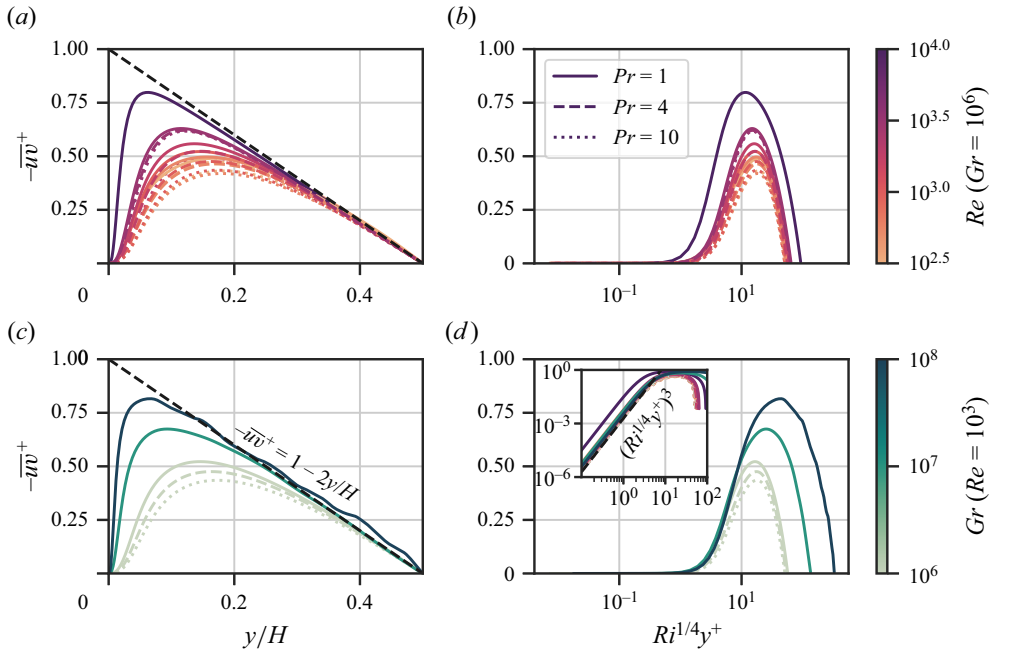

Figure 8. Wall-normal profiles of the streamwise Reynolds stress component $\overline{uv}(y)$ scaled by the streamwise friction velocity $\overline{uv}^+ = \overline{uv}/u_\tau^2$. As in figure 7, (*a*,*b*) are at fixed $Gr = 10^6$ and (*c*,*d*) are at fixed $Re = 10^3$. Colours and line styles are as detailed in the caption of figure 7. (*a*,*c*) Profiles relative to the plate separation H; (*b*,*d*) profiles in viscous wall units scaled by $Ri^{1/4}$. The inset of (*d*) presents the data of (*b*,*d*) with a logarithmic scale on both axes to highlight the near-wall collapse of the data. This figure is also available as an interactive JFM notebook: https://www.cambridge.org/S0022112024005986/JFM-Notebooks/files/Figure-8.ipynb.

streamwise component of the momentum equation (2.1) to obtain

$$\partial_y \overline{uv} = \nu\, \partial_{yy} \bar{u} + \bar{G}, \tag{5.1}$$

where an overbar denotes an average in the periodic (x, z) directions and in time. Note that wall-normal advective fluxes in incompressible channel flows are purely turbulent, i.e. $\overline{uv} \equiv \overline{u'v'}$ since $\bar{v} \equiv 0$. From volume averaging, we can also relate the mean pressure gradient forcing to the mean wall shear stress through $\bar{G} = 2\tau_u/\rho H$. The first integral of (5.1) can therefore be written as

$$\partial_{y^+} \bar{u}^+ - \overline{uv}^+ = 1 - \frac{2y}{H}. \tag{5.2}$$

From (5.1) and (5.2), the close coupling of the mean streamwise velocity and the Reynolds stress $\overline{uv}$ is evident. We therefore present the profiles of $\overline{uv}(y)$ in figure 8. As expected, the Reynolds stress dominates the viscous contribution to (5.2) away from the walls, leading to a balance of $-\overline{uv}^+ \approx 1 - 2y/H$ as shown in figures 8(*a*,*c*). Relative to H, the boundary layer in which the viscous term is relevant becomes thinner as both Re and Gr increase. The near-wall behaviour of $\overline{uv}$ exhibits a remarkable collapse when scaled by $Ri^{1/4}$ as in figures 8(*b*,*d*), except for the highest Re case with $Ri = 0.01$.

The additional factor $Ri^{1/4}$ suggests that the appropriate near-wall length scale for the Reynolds stress is modified from the standard viscous wall unit as

$$Ri^{1/4}y^+ = \frac{y}{l}, \quad l = \frac{\nu}{\sqrt{\dfrac{U_f}{U}\dfrac{\tau_u}{\rho}}}. \tag{5.3a,b}$$

The additional prefactor U_f/U in front of the shear stress suggests that the vertical, convectively driven component of shear cannot be neglected when considering the streamwise Reynolds stress. An improved collapse to that seen in figures 8(*c*,*d*) can be found by computing a viscous length scale using the total shear stress at the wall, $\tau = \sqrt{\tau_u^2 + \tau_w^2}$. As shown explicitly in Appendix A, with this scaling, the Reynolds stress for the highest Re case also matches the other curves. The presence of the convectively driven flow increases the near-wall Reynolds stress, which in turn leads to the flattened mean velocity profiles observed in figure 7(*d*). This result explains qualitatively the origin of the change in C_f with Gr seen in figure 4, where enhanced buoyancy driving led to a larger skin friction. The increase in near-wall Reynolds stress that arises due to convection thins the boundary layer of the mean horizontal velocity, which in turn produces a larger mean gradient at the wall and a larger friction coefficient C_f.

The effect of convection on the shear is by no means a one-way interaction. This is evident from the modification of the mean vertical velocity profile by the imposed horizontal flow. In figures 9(*a*,*b*), vertical velocity profiles are shown for fixed $Gr = 10^6$ and varying Re, with the reference natural convection case ($Re = 0$) highlighted in blue for comparison. Compared to the natural VC case, the introduction of horizontal driving at moderate Re leads to an increase in the peak vertical velocity, and hence an increase in the mean shear both in the bulk and at the walls. At the highest $Re = 10^4$ (the darkest red line in figure 9), a subsequent decrease is observed in the peak vertical velocity, as well as a nonlinear profile in the bulk. None of the cases studied here exhibits a log layer in the vertical velocity, with the largest $\bar{w}^+$ being approximately 6.5 for the most strongly convective case, $Gr = 10^8$. For fixed $Ri = 1$ (shown in figures 9*c*,*d*), all cases show a similar increase in the peak velocity, and the mean gradient in the bulk appears largely independent of Gr and Pr. The distance of the velocity peak from the wall (compared to the channel width H) decreases for larger Gr, but the value of the peak velocity in free-fall units does not depend strongly on Gr. This similarity at constant Ri is suggestive that the vertical velocity modification is determined primarily by the relative strength of the horizontal flow to convection.

To further investigate the behaviour of the vertical velocity profiles, we now turn to the mean vertical momentum budget. Unlike the streamwise velocity in (5.1)–(5.2), the vertical velocity is not only tied to the Reynolds stress profile. Rather, the mean vertical momentum equation reads

$$\partial_y \overline{vw} = \nu\, \partial_{yy}\bar{w} + g\alpha\bar{\theta}. \tag{5.4}$$

Close to the wall, we expect the Reynolds stress to be negligible and a balance to arise between buoyancy and viscosity. Due to the symmetry of the boundary conditions, all three terms must be zero at the channel centre. In the bulk of the flow, the mean velocity is approximately linear, so we expect a balance between buoyancy and Reynolds stress. These features are present in each of the simulations highlighted in figure 10. As Re increases, the key modification to the budget arises in the Reynolds stress term $-\partial_y \overline{vw}$. In natural VC, there is a minuscule positive peak in the Reynolds stress term close to the wall, but

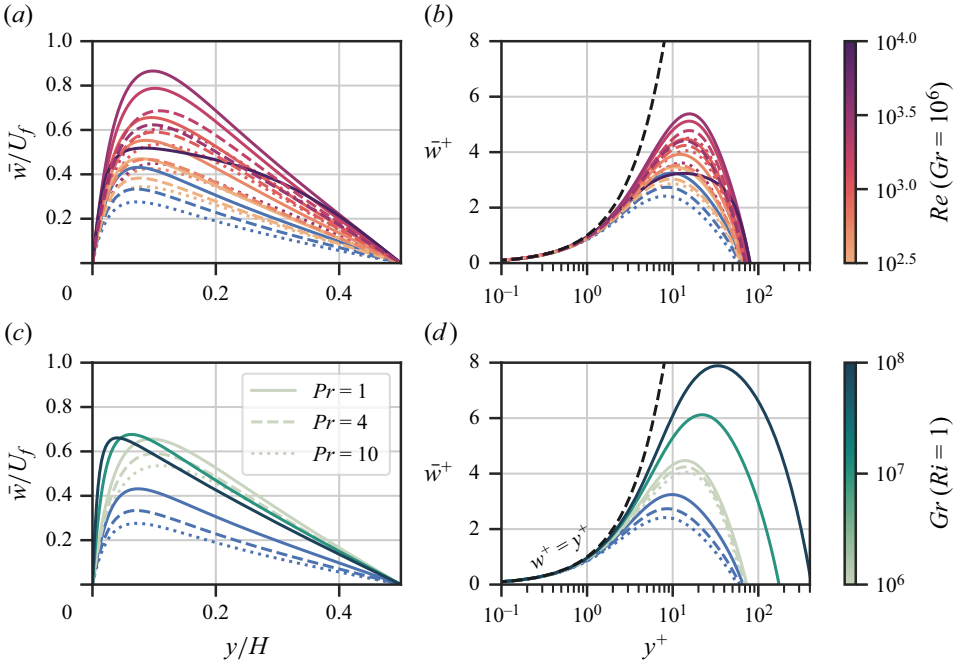

Figure 9. Mean profiles of the vertical velocity $\bar{w}(y)$. As in figure 7, (*a*,*b*) are at fixed $Gr = 10^6$, but here (*c*,*d*) are at fixed $Ri = 1$. (*a*,*c*) Profiles are normalised by the free-fall velocity $U_f = \sqrt{g\alpha\,\Delta H}$ and the plate separation H. (*b*,*d*) Profiles are presented in viscous wall units, where $\bar{w}^+ = \bar{w}/w_\tau$ and $y^+ = yw_\tau/\nu$. Reference data for natural VC (with $Gr = 10^6$, $Re = 0$) are shown in blue. This figure is also available as an interactive JFM notebook: https://www.cambridge.org/S0022112024005986/JFM-Notebooks/files/Figure-9.ipynb.

its amplitude is so small that it is indistinguishable in figures 10(*a*,*f*). This peak grows with Re, becoming visible at $Re = 10^{3.5}$ in figures 10(*d*,*i*), coinciding with a flattened profile of the viscous term (shown in green). By $Re = 10^4$, at which the Reynolds stresses are significantly energised by the horizontal forcing, the nonlinear term peak exceeds the contribution from the buoyancy term. This leads to a significant drop in the viscous term at $y \approx 10^{-2}H$, which determines the modified mean velocity observed in figures 9(*a*,*b*).

Changes in the mean temperature profile $\bar{\theta}$ in figure 10 are more subtle, with the most obvious feature being a slight drop in figure 10(*e*), coinciding with the Reynolds stress peak. A clearer picture of the mean temperature response can be found in figure 11, where profiles are plotted both on linear axes and in wall units. Since the dimensionless wall temperature gradient is equivalent to the Nusselt number, which is most strongly dependent on Ra, we compare the temperature profiles in figures 11(*a*,*b*) at varying Re and Pr but fixed $Ra = 10^7$. As shown in these plots, the temperature gradient in the bulk increases with Re, and any possible log-law profile does not collapse to a universal slope or coefficient. For fixed $Ri = 1$, however, shown in figures 11(*c*,*d*), the bulk gradient appears independent of Gr, suggesting that Ri and Pr are the key control parameters determining the flow properties away from the walls.

The mean profiles presented here do not further clarify the origin of the non-monotonic behaviour of Nu with Re seen in figure 6. When normalised by the wall heat flux, the mean temperature profiles in figure 11(*b*) show a monotonic increasing trend with Re away from the wall. The non-monotonic behaviour observed in the vertical velocity profiles of figures 9(*a*,*b*) suggests an intrinsic connection between the vertical flow and the

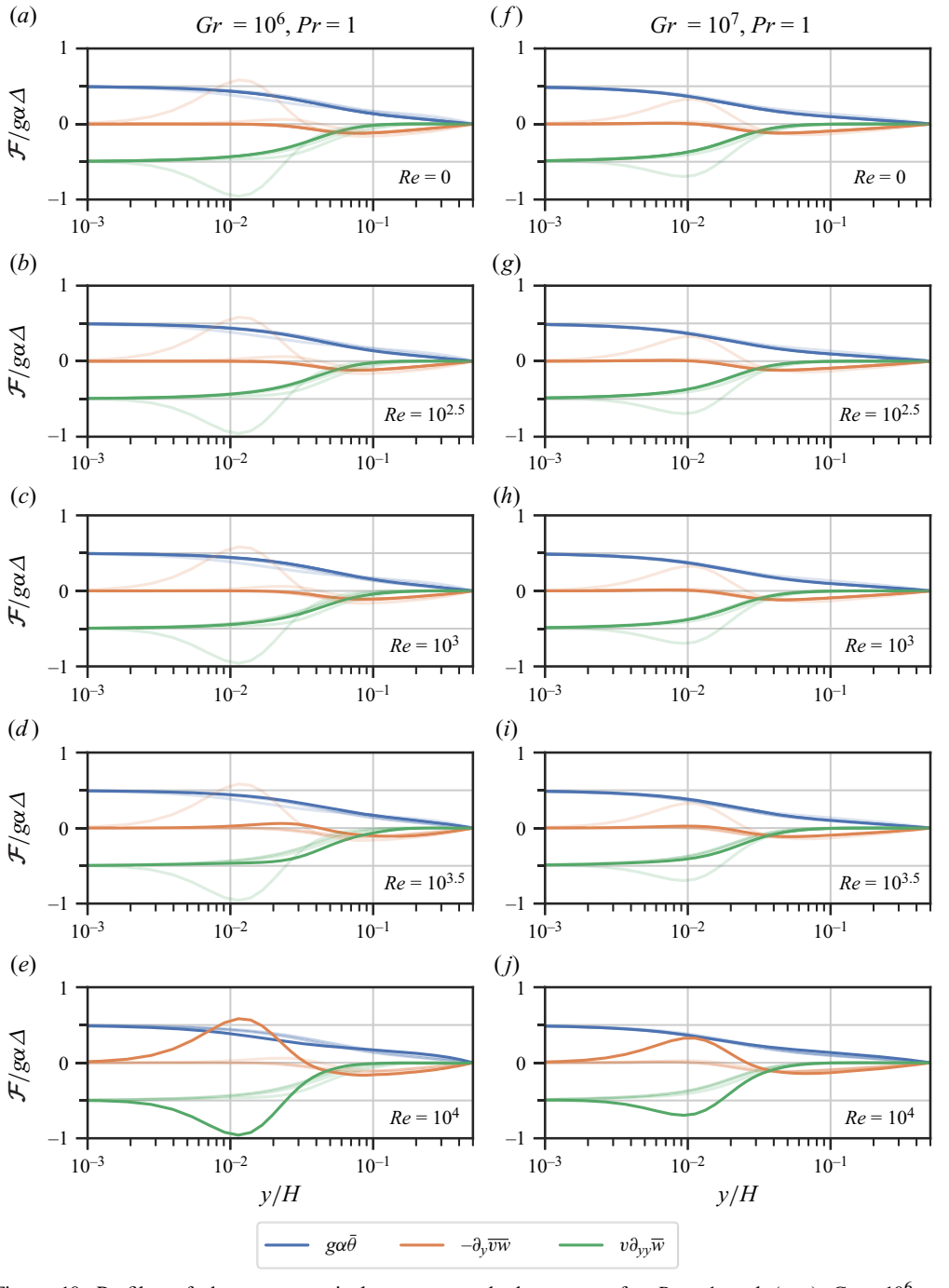

Figure 10. Profiles of the mean vertical momentum budget terms for $Pr = 1$ and (*a–e*) $Gr = 10^6$ or (*f–j*) $Gr = 10^7$. Reynolds numbers vary from (*a*,*f*) $Re = 0$ to (*e*,*j*) $Re = 10^4$. Colours denote the budget term being plotted as detailed in the legend, and each budget term is plotted normalised against the buoyancy scale $g\alpha\Delta$. Within each column, semi-transparent lines are added to show the profiles for the Reynolds numbers highlighted by the other rows as comparison. The wall-normal coordinate y is plotted on a logarithmic axis to highlight the variation in the near-wall region. This figure is also available as an interactive JFM notebook: https://www.cambridge.org/S0022112024005986/JFM-Notebooks/files/Figure-10.ipynb.

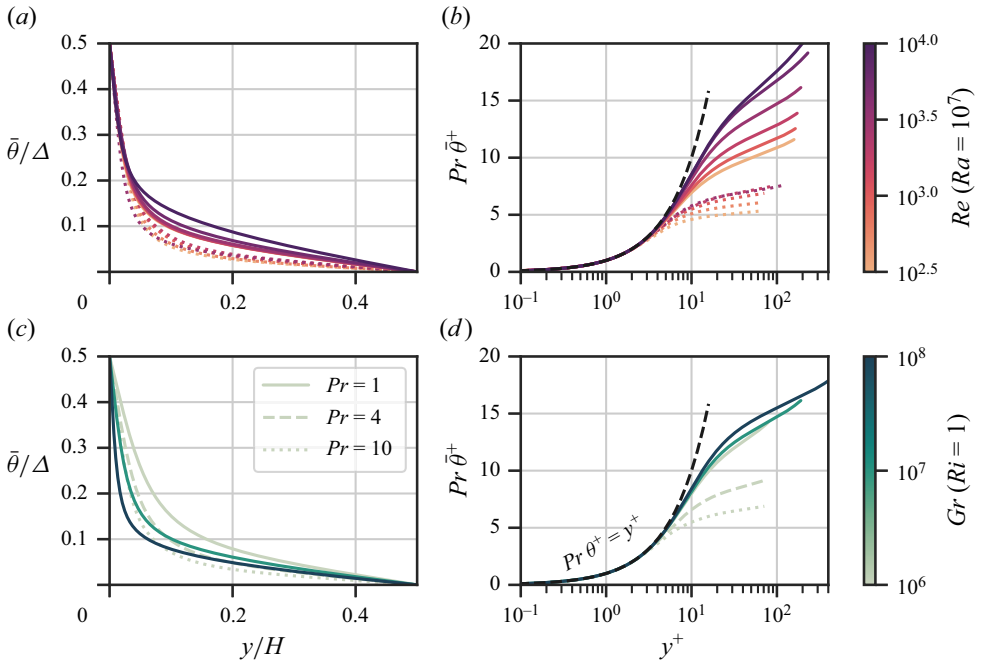

Figure 11. Mean temperature profiles for (*a*,*b*) fixed $Ra = 10^7$ and (*c*,*d*) fixed $Ri = 1$. As in figures 7–9, colours denote changes in Re and Gr, whereas line styles show changes in Pr. (*a*,*c*) Temperature is normalised by the difference across the plates Δ. (*b*,*d*) Temperature is shown in terms of wall units $\theta^+ = (\theta_w - \theta)U_\tau/F_\theta$, where θ_w is the temperature at the wall $y = 0$. The U_τ value used here and in $y^+ = yU_\tau/\nu$ is calculated using both components of the wall shear stress, as defined in (A1). This figure is also available as an interactive JFM notebook: https://www.cambridge.org/S0022112024005986/JFM-Notebooks/files/Figure-11.ipynb.

wall-normal heat transport, although the very subtle changes in the vertical momentum budget remain difficult to interpret in the context of the non-monotonic Nusselt number variation. The later sections on spectral analysis and statistics of the boundary layer aim to shed more light on this global heat transport.

To conclude our analysis of the mean profiles, we compare the new simulations of mixed VC to the universal functions of the MOST (Monin & Obukhov 1954; Foken 2006). As outlined in the Introduction, the theory considers a region of the flow where viscosity and molecular diffusion are negligible, and the appropriate length scale is the Obukhov length

$$L_O = \frac{u_\tau^3}{g\alpha F_\theta}. \tag{5.5}$$

On dimensional grounds, universal functions that depend only on y/L_O for the first- and second-order statistics can then be constructed for the temperature and velocity fields. One key assumption used to derive the universal functions for velocity is that the turbulent momentum flux $\rho\,\overline{uv}$ is constant over the region of interest. However, as shown in figure 8, this is not true in a turbulent channel flow driven by a pressure gradient, where the Reynolds stress follows a linear relation in the bulk. We can therefore expect the universal functions of Monin & Obukhov (1954) to hold for only a small range of y in our simulations.

Considering these caveats, we present a collection of mean profiles from the mixed VC simulations as a function of y/L_O in figure 12. Following Pirozzoli *et al.* (2017), who

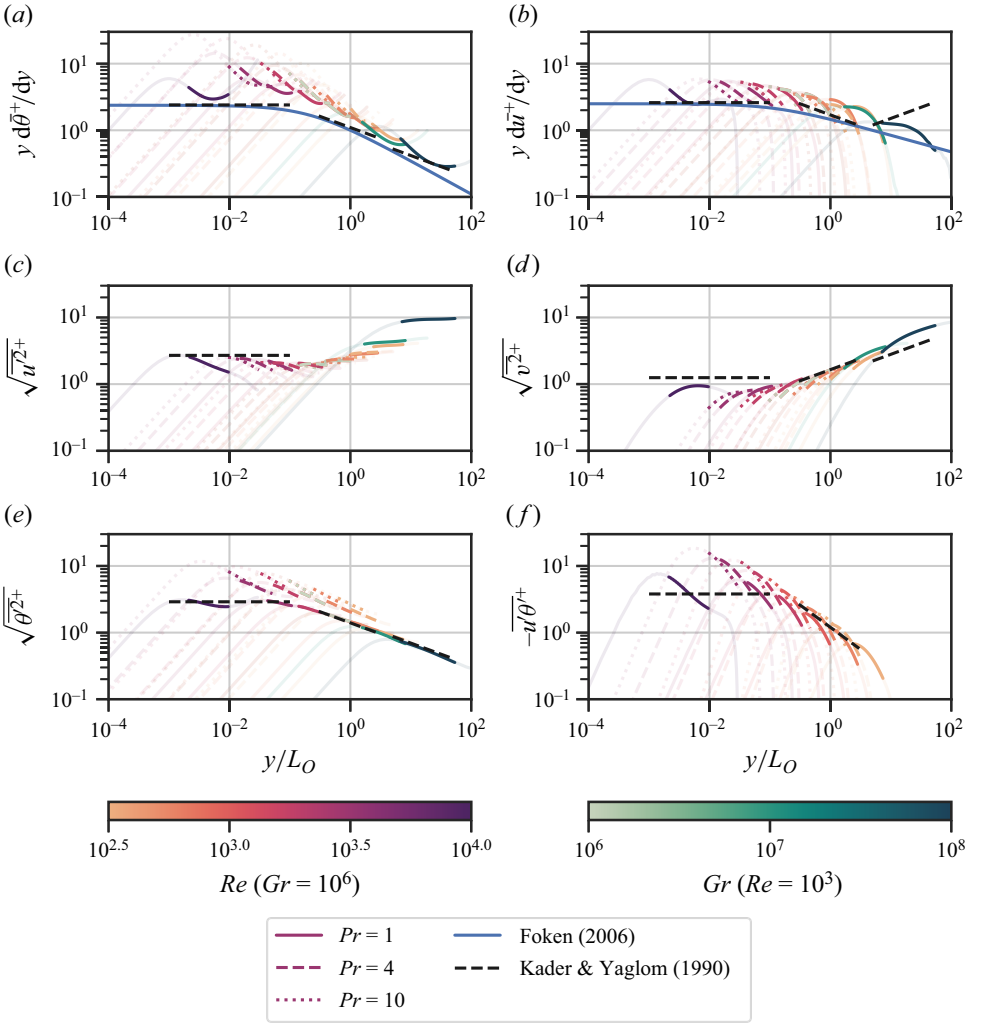

Figure 12. Comparison of the mixed VC simulation results with the 'universal functions' of the MOST for first- and second-order statistics. Profiles are shown as semi-transparent unless the advective wall-normal fluxes of heat $\overline{v\theta}$ and momentum $\overline{vu}$ are within 80 % of their maximum value. Consistent with the Monin–Obukhov formulation, all quantities here are normalised by the horizontal component of the friction velocity u_τ and the wall-normal heat flux F_θ. This figure is also available as an interactive JFM notebook: https://www.cambridge.org/S0022112024005986/JFM-Notebooks/files/Figure-12.ipynb.

present a similar figure (their figure 16) for mixed RB convection, we emphasise only the region of the domain where the turbulent fluxes of heat and momentum are greater than 80 % of their maximum value, with the rest of the profiles made semi-transparent. We compare our results with the updated scaling theories of Kader & Yaglom (1990), and for the mean temperature and velocity profiles, the commonly used Businger–Dyer relations outlined in Foken (2006). For the highlighted region where the fluxes are close to their peak, the majority of the results collapse onto a single function of y/L_O close to these profiles. In figure 12(*a*), there are two notable discrepancies from the theoretical estimates for the mean temperature profile. First, the values at transitional $y/L_O \approx 10^{-1}$ are approximately a factor 2 larger than the suggested profiles. Second, the effective power-law scaling observed for strong buoyancy driving $y \geq L_O$ appears steeper than the

$-1/3$ proposed by Kader & Yaglom (1990) (dashed black lines), and closer to the $-1/2$ scaling associated with the asymptotic limit of the Businger–Dyer relation (solid blue line). A discrepancy in the two theoretical predictions for the mean velocity profile at $y \gg L_O$, highlighted in figure 12(*b*), cannot be resolved from the results presented here, although we note that the data here agree well with the mixed RB data of Pirozzoli *et al.* (2017). The variation in Pr across the simulations collapses for most quantities in figure 12, except for the r.m.s. temperature shown in figure 12(*e*). The origin of this discrepancy with Pr is currently unclear, but understanding how the Pr dependence may affect the Monin–Obukhov profiles is important in the context of their applications outside the atmosphere, for example in the surface layer of the upper ocean (Zheng, Harcourt & D'Asaro 2021).

6. Spectral analysis

We now investigate the scale dependence of the thermal structures and heat flux in mixed convection through analysis of the power spectra. To ensure that we capture the full range of dynamical scales, we perform further simulations in extended aspect ratio domains, with $L_x = L_z = 24H$. The details of these simulations are outlined in table 2 of Appendix B.

In unsheared RB convection, Krug, Lohse & Stevens (2020) show that large-scale patterns, also known as superstructures, can be identified from a low-wavenumber peak in the power spectrum of the temperature field and in the co-spectrum of the wall-normal heat flux. This peak denotes the scale of the large-scale circulation or 'wind' of convection that is key to theories describing RB convection. Since there is no preferential horizontal flow direction in RB convection, one-dimensional spectra can be analysed, but in mixed VC, the two directions parallel to the plates must be considered separately.

We therefore compute time-averaged spectra using two-dimensional Fourier transforms in the periodic directions. For visualisation purposes, we present separate one-dimensional spectra for the streamwise (x) and spanwise (z) wavenumbers, which are computed by integrating over the other wavenumber. Precisely, the two- and one-dimensional co-spectra of any two variables f and g are defined as

$$\Phi_{fg}(k_x, y, k_z) = \mathrm{Re}[\hat{f}^* \hat{g}], \quad \Phi_{fg}(k_x, y) = \int \mathrm{Re}[\hat{f}^* \hat{g}] \, \mathrm{d}k_z, \tag{6.1a,b}$$

where $\hat{f}$ denotes the two-dimensional Fourier transform of f in x and z, and Re denotes the real part. The Fourier transforms are normalised such that integrating the spectrum over wavenumber space recovers the corresponding volume-averaged quantity $\langle fg \rangle = \iint \Phi_{fg} \, \mathrm{d}k_x \, \mathrm{d}k_z$.

The power spectrum of temperature $\Phi_{\theta\theta}$ is presented in figure 13 for the four extended simulations. In figure 13(*a*), for the standard RB configuration, we see behaviour similar to that in Krug *et al.* (2020), with a distinct, sharp low-wavenumber peak at $kH \approx 1$, and a more broad peak at smaller scales. As mentioned above, the lack of a preferential direction means that the two directional spectra are virtually identical. When shear is added to the RB system in figure 13(*b*), the horizontal isotropy in the system is destroyed. As expected from previous work on mixed RB (Pirozzoli *et al.* 2017; Blass *et al.* 2020, 2021; Yerragolam *et al.* 2022), coherent rolls aligned with the streamwise axis dominate the signal. Note the difference in y axis between figures 13(*a*) and13(*b*). In the streamwise spectrum $\Phi_{\theta\theta}(k_z, y)$, a sharp peak at $kH \approx 2$ is visible at all wall-normal locations, but is particularly prominent in the near-wall region (light green) where there is a maximum in $\overline{\theta^2}(y)$. The corresponding wavelength of these structures is $\lambda = 2\pi H/k_z \approx 3H$, which is

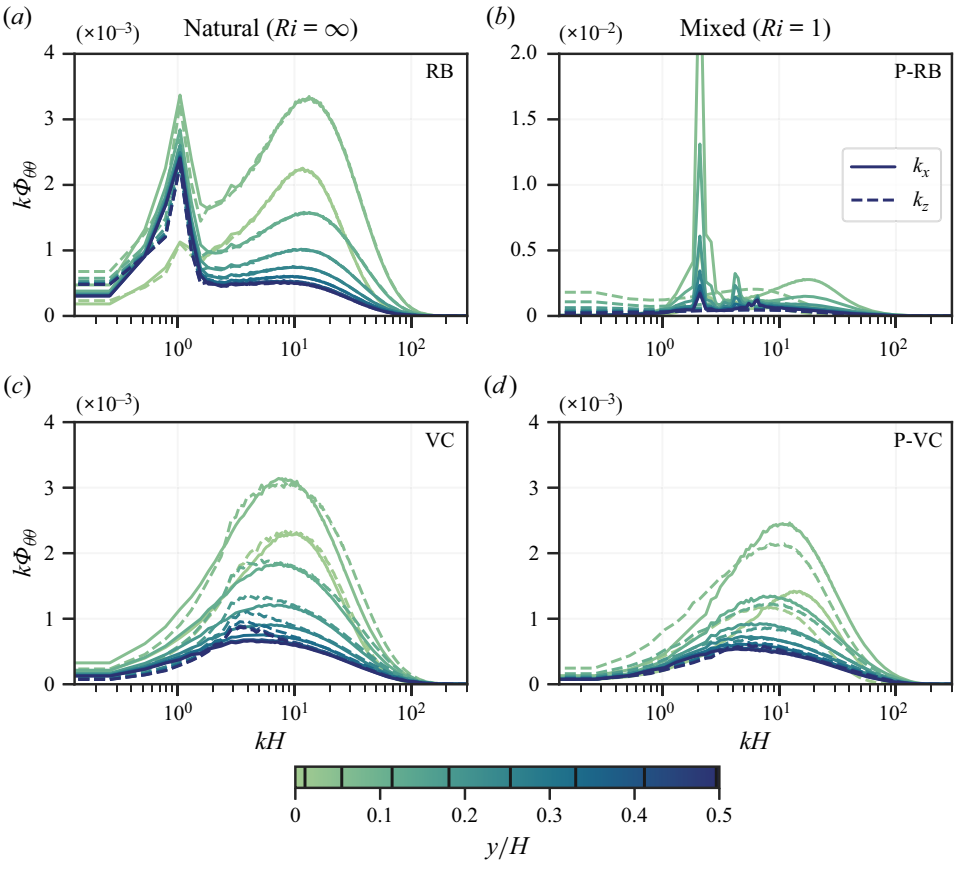

Figure 13. One-dimensional power spectra $\Phi_{\theta\theta}(k, y)$ of temperature for the extended domain simulations described in table 2. Solid lines denote spectra as functions of $k = k_x$, and dashed lines are functions of $k = k_z$. The colour of each line is determined by its wall normal location y, with the specific locations highlighted on the colour bar. Each spectrum is multiplied by the wavenumber k such that area under each curve is representative of the relative contribution in wavenumber space. (*a*,*c*) Simulations of natural convection ($Re = 0$). (*b*,*d*) Simulations of mixed convection at $Ri = 1$. (*a*,*b*) The RB cases with gravity in the wall-normal (y) direction. (*c*,*d*) The VC cases with gravity parallel to the wall in z. Note that P-VC here denotes the Poiseuille-VC configuration to compare with P-RB. All simulations have fixed $Gr = 10^7$, $Pr = 1$. This figure is also available as an interactive JFM notebook: https://www.cambridge.org/S0022112024005986/JFM-Notebooks/files/Figure-13.ipynb.

consistent with that observed previously in the mixed convection literature at $Ri = 1$ (e.g. Pirozzoli *et al.* 2017). The alignment of the flow structures in the streamwise direction leads to a broad contribution to the streamwise spectrum at low k_x. This behaviour is purely a result of the regular alignment, and is not related to any domain size effects.

In figures 13(*c*,*d*), we present the same analysis but for natural and mixed vertical convection. The contrast to the RB cases is immediately apparent, with no sharp peaks at any wavenumber or wall-normal position. This confirms the earlier visual observation of figure 3, where the instantaneous snapshots showed no clear coherent length scale. In natural VC, shown in figure 13(*c*), the two one-dimensional spectra do not overlap exactly as in the RB case due to the buoyancy-driven mean flow in the vertical. The k_x spectrum shows a small peak at $kH \approx 3$ that is absent from the k_z spectrum and becomes more prominent towards the channel centre. Comparing figures 13(*c*) and 13(*d*), we see

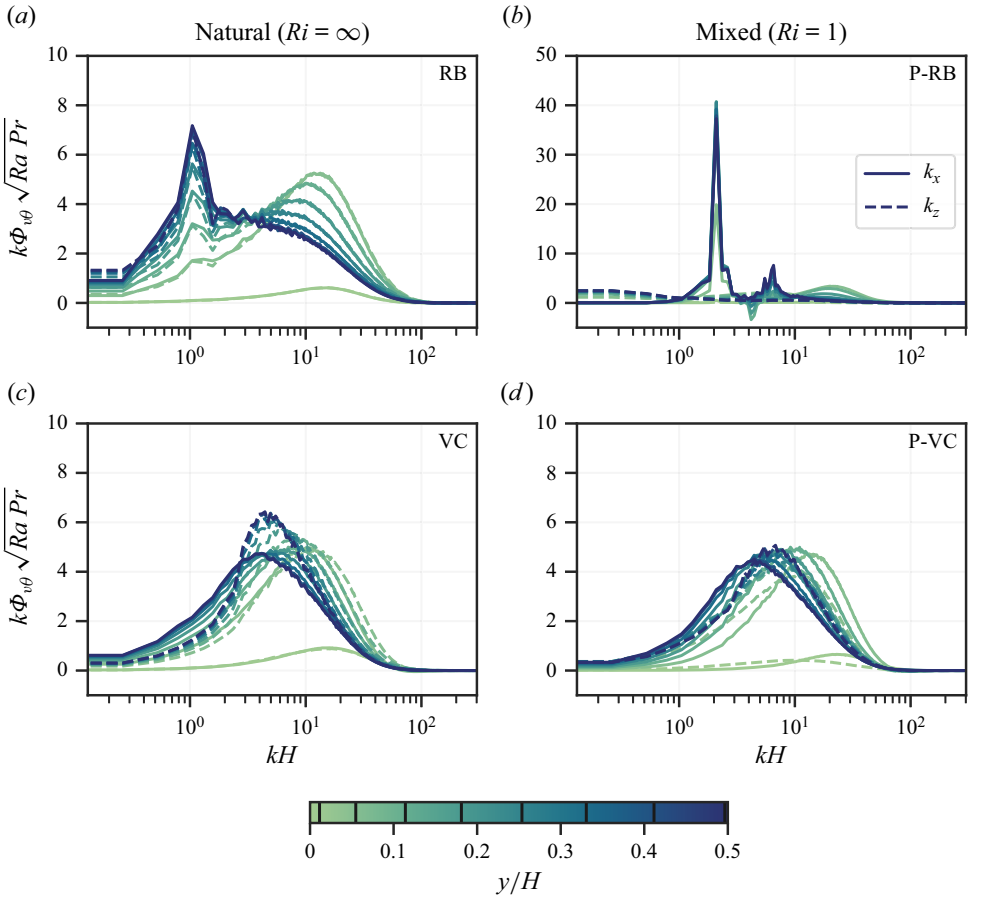

Figure 14. One-dimensional co-spectra $\Phi_{v\theta}(k, y)$ of the wall-normal heat flux for the extended domain simulations described in table 2. See the caption of figure 13 for more details on the meanings of line styles and colours. The spectra are normalised by $\sqrt{Ra\,Pr}$ such that integration over k recovers the dimensionless advective heat flux $Nu - 1 = \langle v\theta \rangle / (\kappa \Delta / H)$. As in figure 13, the configurations presented are (*a*) RB, (*b*) mixed RB, (*c*) VC, (*d*) mixed VC. This figure is also available as an interactive JFM notebook: https://www.cambridge.org/S0022112024005986/JFM-Notebooks/files/Figure-14.ipynb.

that this peak is suppressed by the addition of external shear. Furthermore, all of the broad mid-range peaks in the spectra exhibit a decrease in amplitude and a shift to higher wavenumbers.

The heat flux co-spectra $\Phi_{v\theta}$, shown in figure 14, exhibit similar features to the power spectra. In figures 14(*a*,*b*), a sharp low-wavenumber peak is once again visible for RB and mixed RB systems, and for the heat flux, this peak increases towards the channel centre. A broad high-wavenumber peak is also observed in the spectrum close to the wall. This peak flattens and shifts to lower wavenumbers (i.e. larger scales) as distance from the wall increases, which can be interpreted as the emergence and coalescence of small-scale plume structures. A similar behaviour can be found in the VC configurations of figures 14(*c*,*d*), with the broad peak in both the k_x and k_z spectra shifting to lower wavenumbers for larger y. However, in the k_x spectrum for natural VC (where x is perpendicular to gravity), this peak also increases in amplitude towards the channel centre, highlighting that the majority of the wall-normal heat transport at the channel centre occurs due to structures of size $\lambda \approx H$. Comparing this to the mixed VC case in

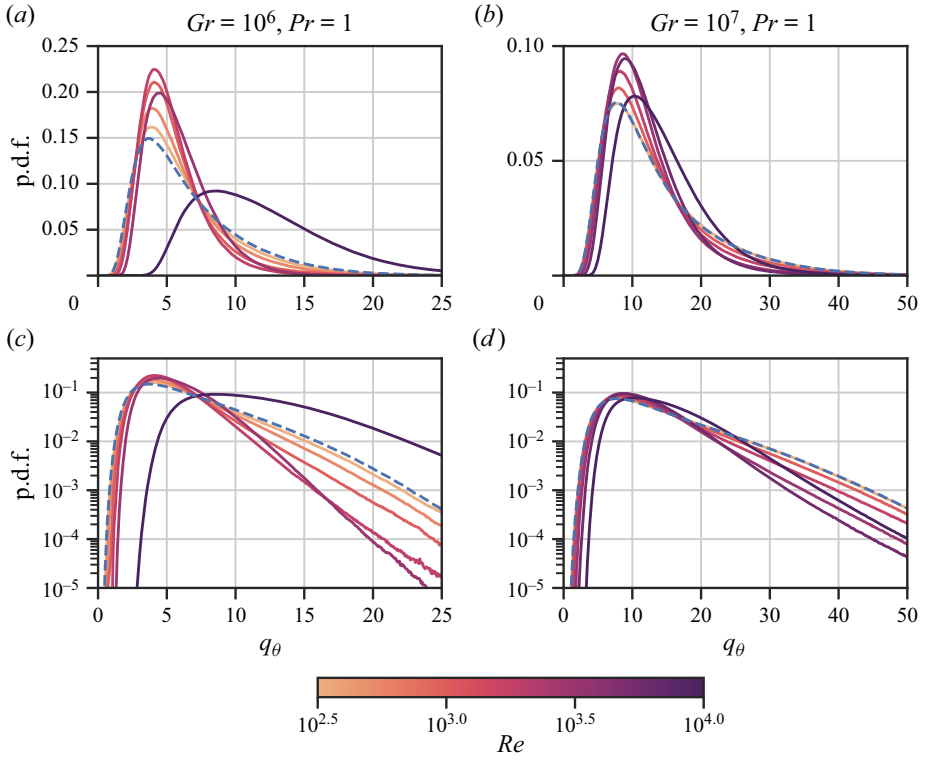

Figure 15. Probability density functions (p.d.f.s) of the dimensionless local heat flux q_θ as defined in (3.1) for (*a*,*c*) $Gr = 10^6$ and (*b*,*d*) $Gr = 10^7$. Line colours highlight variation in the Reynolds number, as shown by the colour bar, with the blue dashed line plotting the data for natural convection with $Re = 0$. Plots (*a*,*b*) are presented with linear y axes, and (*c*,*d*) present the same data on logarithmic y axes to highlight the exponential tails. This figure is also available as an interactive JFM notebook: https://www.cambridge.org/S0022112024005986/JFM-Notebooks/files/Figure-15.ipynb.

figure 14(*d*), the mid-scale peak appears significantly suppressed when the external shear is imposed, suggesting that the coalescence of plumes in the bulk is disrupted by the shear. This is consistent with the interpretation of Domaradzki & Metcalfe (1988) and Scagliarini *et al.* (2014), who argued that the drop in heat flux in mixed RB can be related phenomenologically to disruption of the organisation of small-scale convective plumes.

7. Heat flux statistics in the boundary layer

Whereas the previous section focused on the advective heat flux in the bulk and its modification due to shear, we now turn to the conductive heat flux that dominates the transport in the boundary layer. Specifically, we investigate the statistical distribution of the local conductive heat flux at the boundary plates. As defined earlier, in (3.1), we consider the local dimensionless heat flux q_θ whose time and plane average is equivalent to the Nusselt number. The pointwise data of $q_\theta(x, z, t)$, also shown in figure 2, are collected over time and space to construct histograms that are normalised to produce probability density functions (p.d.f.s) in figure 15. The data shown here are only for $Pr = 1$ and $Gr = 10^6$, 10^7 since these cases cover the widest range of Richardson numbers, highlighting the transition from natural convection to forced convection.

In figures 15(*a*,*b*), where the data are presented on linear axes, we find the same effect of increasing shear at both Grashof numbers. As Re increases from zero (shown by

progressively darker lines, with $Re = 0$ marked in blue for comparison), the peak of the p.d.f. increases in amplitude. In statistical terms, this means that the most common values of local heat flux become more common as shear is increased, up to $Re \approx 10^{3.5}$. Due to the skewed nature of the distributions, these increasingly common values of heat flux are below the mean, and although the peak shifts slightly to the right as Re increases, these parameters are associated with the drop in heat flux observed in figure 6. This corresponds to the visualisation of figure 2, where the streaks of low heat flux span a larger proportion of the boundary at $Ri = 1$ (figures 2*e*,*i*) than at high Ri (figures 2*b*,*c*). Once Re is sufficiently high, which in these cases is for $Re > 10^{3.5}$, the whole distribution shifts more significantly to higher q_θ as the transport becomes dominated by the pressure-driven shear flow.

At moderate Re, another key modification is to the tails of the distribution. These are visualised most clearly in figures 15(*c*,*d*), where the heat flux distributions are plotted on a logarithmic axis. In this representation, it is clear that the right tails of large heat flux decay exponentially for $Gr = 10^7$, and close to exponentially for $Gr = 10^6$. At both Grashof numbers, the tails are reduced as Re increases relative to the natural convection case, showing that the probability of extreme local heat flux values is reduced due to the introduction of a mean horizontal flow. Again, this is consistent with what was observed in the visualisation of figure 2, where dark patches associated with large local heat flux became less prevalent as Re increases. In natural VC, Pallares *et al.* (2010) used conditional sampling to show that these patches are most often associated with instantaneous flow reversals at the walls, which are likely a result of impacting plumes originating from the opposing wall.

8. Conclusion and outlook

In this paper, we have investigated mixed convection in a differentially heated vertical channel subject to a horizontal pressure gradient, referred to as mixed vertical convection (VC), through direct numerical simulations. By simulating the system across the parameter ranges $10^6 \leq Gr \leq 10^8$, $1 \leq Pr \leq 10$ and $10^{2.5} \leq Re \leq 10^4$, we have explored the transition from natural convection to forced convection, characterised by the Richardson number $10^{-2} \leq Ri \leq 10^2$. Across this parameter range, the response of the streamwise skin friction is identical to the response seen in mixed Rayleigh–Bénard (RB) convection, with a power-law Re dependence for C_f giving way to the Prandtl friction law (4.2) at sufficiently high Re. The presence of convection acts to increase the skin friction for a given Re, due to the thermal plumes emitted from the plates, with a collapse observed for all the data in the power-law regime $C_f \sim Gr^{1/4}Re^{-\gamma}$ for both configurations across the entire range of Pr. For mixed VC, the streamwise momentum budgets show an enhanced impact of Reynolds stresses close to the wall at higher Ri, which modify the shape of the mean velocity profile. The Reynolds stresses in the boundary layer are driven by the combined shear stress of the horizontal pressure-driven flow and the VC flow.

Friction coefficients could also be obtained for the flow component associated with buoyancy driving. For cases with significant buoyancy effects at $Ri > 1/4$, a reasonable collapse was found for the laminar-like scaling $C_f \sim Re_\delta^{-1}$ where Re_δ is the boundary layer Reynolds number of the convection flow. The introduction of the horizontal pressure gradient leads to significant modification of the mean vertical velocity, with Re_δ increasing up to three times its value for natural convection, and a corresponding increase in the mean shear in the channel bulk for moderate Re. For $Ri = O(1)$, the response of the Nusselt number Nu to the introduction of shear in mixed VC is also identical to that in mixed

RB. Before the flow undergoes a transition to a forced convection regime at high Re, the response can be expressed as $Nu/Nu_0 = f(Re/Re_0)$, where Nu_0 and Re_0 are the Nusselt number and Reynolds number associated with natural convection. The data of both mixed convection systems collapse onto this single curve, which describes the drop in Nu as Re increases.

The near identical quantitative response of mixed RB and mixed VC is observed despite striking qualitative differences between the two configurations in terms of large-scale flow organisation. Whereas mixed RB features large convective rolls oriented along the streamwise axis, no such structures form in mixed VC except at low Ri when the dynamics are dominated solely by the pressure gradient forcing. The absence of a low-wavenumber peak in the heat flux co-spectrum for mixed VC confirms that the advective heat flux across the domain is transported by eddies or plumes with a wide range of scales rather than by large coherent rolls. Comparing the spectra from natural VC with mixed VC reveals that the organisation of plume structures with a horizontal scale $\lambda \approx H$ is suppressed by the horizontal mean flow. This is reflected also in the distribution of local heat flux at the boundaries, which shows that instantaneous events of extreme heat flux become less likely as Re increases. As the boundaries become dominated by streaky structures, the formation of localised plume structures is disrupted, consistent with the earlier interpretations of reduced heat flux in mixed RB (Domaradzki & Metcalfe 1988; Scagliarini *et al.* 2014).

The striking agreement between the two channel configurations compared here, regardless of the gravity direction, opens up the question of how universal such a response in skin friction and heat flux is for other mixed convection systems. The independence to the gravity direction suggests that our results may be applicable more generally to inclined layer convection, as studied by Daniels & Bodenschatz (2002) at low Gr, subject to a horizontal pressure gradient at comparable Gr and Re. However, it is less clear how directly applicable the findings here are to a wall plume subject to a crossflow. Such a scenario is relevant to environmental applications such as at a melting ice face subject to ambient ocean currents (Jackson *et al.* 2020). Whereas both boundaries impact the transport in mixed RB and mixed VC, a wall plume constantly entrains fluid from the ambient at its outer edge. Recent work has provided an innovative way to simulate wall plumes at high Gr, through studying temporally growing boundary layers (Ke *et al.* 2023; Wells 2023), and it would be fruitful to understand how the growth of these boundary layers is affected by the presence of a turbulent crossflow. For ice–ocean interactions, the picture is further complicated through multicomponent transport (Howland, Verzicco & Lohse 2023) and the development of rough boundaries that are closely coupled to the flow structures (Couston *et al.* 2021; Ravichandran, Toppaladoddi & Wettlaufer 2022).

From a more theoretical standpoint, our current work has also emphasised how certain flow properties are noticeably modified under the transition from natural VC to forced convection. These include the sign of the near-wall Reynolds stress in figure 10 and the distribution of the local wall heat flux in figure 15. In both RB and VC, predictions have been made for a transition to the 'ultimate' regime at sufficiently high buoyancy driving, where the boundary layers behave as turbulent boundary layers (Lohse & Shishkina 2023), although this regime has thus far been inaccessible to three-dimensional numerical simulation. Analysis of the aforementioned statistical quantities in natural convection at high Gr may help in identifying key markers of such a transition in natural convection systems.

Supplementary material. Computational Notebook files are available as supplementary material at https://doi.org/10.1017/jfm.2024.598 and online at https://www.cambridge.org/S0022112024005986/JFM-Notebooks.

Acknowledgements. We are grateful to E. Ching for fruitful discussions about natural vertical convection, and to O. Shishkina and R. Stevens for insights into the response of mixed Rayleigh–Bénard convection. We would also like to thank three anonymous referees for their insightful comments on this paper.

Funding. The work of C.J.H. was funded by the Max Planck Center for Complex Fluid Dynamics. The contribution of G.S.Y. towards this project has received funding from the European Research Council under the European Union's Horizon 2020 research and innovation program (grant no. 804283). We acknowledge PRACE for awarding us access to Irene at Très Grand Centre de Calcul (TGCC) du CEA, France (project 2021250115). For the extended domain simulations, the authors also gratefully acknowledge the Gauss Centre for Supercomputing e.V. (www.gauss-centre.eu) for funding this project (pr74sa) by providing computing time on the GCS Supercomputer SuperMUC-NG at Leibniz Supercomputing Centre (www.lrz.de). This work was also carried out on the Dutch national e-infrastructure with the support of SURF Cooperative.

Declaration of interests. The authors report no conflict of interest.

Author ORCIDs.
Christopher J. Howland https://orcid.org/orcid.org/0000-0003-3686-9253;
Guru Sreevanshu Yerragolam https://orcid.org/0000-0002-8928-2029;
Roberto Verzicco https://orcid.org/0000-0002-2690-9998;
Detlef Lohse https://orcid.org/0000-0003-4138-2255.

Appendix A. Alternative near-wall scaling for the streamwise Reynolds stress

As shown in figures 8(*b*,*d*), the near-wall profile of the streamwise Reynolds stress $\overline{uv}^+(y^+)$ requires an additional prefactor $Ri^{1/4}$ to collapse the majority of the cases studied here. In § 5, we attribute this to the multiple components of shear at the wall that produce the Reynolds stress, which cannot be captured by the streamwise component u_τ alone. This is confirmed in figure 16, where we re-plot $\overline{uv}^+$ against a wall-normal coordinate scaled with the total shear stress at the wall. Specifically, we scale with the viscous wall unit ν/U_τ, where the total friction velocity U_τ satisfies

$$U_\tau = \sqrt{\frac{|\boldsymbol{\tau}|}{\rho}} = \left(\frac{\sqrt{\tau_u^2 + \tau_w^2}}{\rho}\right)^{1/2} = (u_\tau^4 + w_\tau^4)^{1/4}. \tag{A1}$$

Compared to the results of figure 8, the previously outlying case $Re = 10^4$ (plotted as a dark purple line) now also shows a reasonable collapse with the rest of the data in the near-wall region of figure 16. This result highlights the intricate nature of turbulence in mixed VC, with different friction velocities needed to scale the two axes of figure 16 to describe the Reynolds stress. Although the near-wall length scale is determined by the total shear stress in (A1), the Reynolds stress must still satisfy the global balance (5.2), where u_τ is the relevant velocity scale.

Appendix B. Simulation parameters

Table 1 details the physical and numerical input parameters used for the mixed VC simulations. Even at $Pr = 1$, we use a more refined grid for the temperature field since sharper gradients can emerge than in the velocity field due to the lack of a pressure gradient term in (2.2) when compared with (2.1).

In § 6, an additional set of simulations is discussed in which the periodic extent of the domain is tripled to an aspect ratio $\Gamma = 24$. In that section, we compare RB configurations with gravity aligned normal to the boundary plates (in the negative y direction) to VC configurations where gravity is aligned parallel to the plates (in the negative z direction).

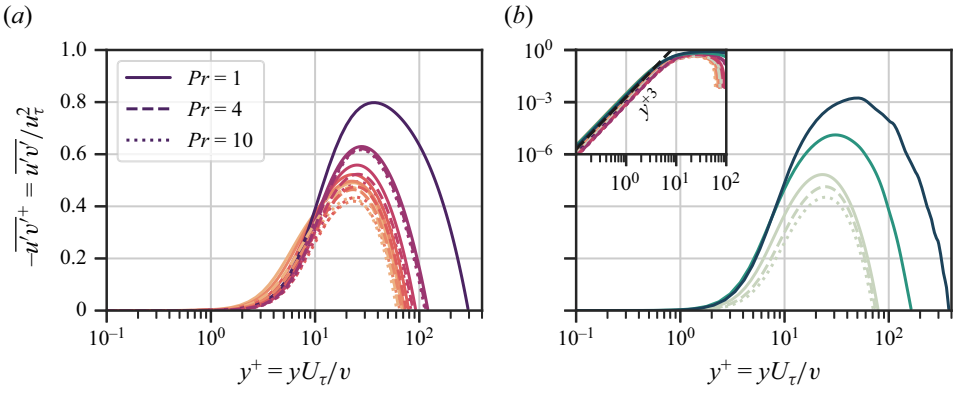

Figure 16. Wall-normal profiles of the streamwise Reynolds stress $\overline{uv}$ normalised by the streamwise friction velocity u_τ as shown previously in figure 8. Here, the wall-normal coordinate y is scaled by the viscous wall unit ν/U_τ computed from the total wall shear stress $|\boldsymbol{\tau}|$. Data (*a*) at fixed $Gr = 10^6$, with (*b*) at fixed $Re = 10^3$, and the same colours and line styles as in figure 8, are used to denote variation in Gr, Re and Pr. As in figure 8, the inset presents both sets of data with a logarithmic scale on both axes. This figure is also available as an interactive JFM notebook: https://www.cambridge.org/S0022112024005986/JFM-Notebooks/files/Figure-16.ipynb.

Table 2 details the input parameters used for these additional simulations. Recall that a prefix 'P-' in the name of a simulation denotes the presence of a Poiseuille-like pressure gradient forcing.

Appendix C. Kinetic energy budgets

For completeness, we finally provide an overview of the volume-averaged kinetic energy budgets for the pressure-driven mixed convection in a vertical channel. All of the data presented here, along with additional second-order statistics, may be found in the online JFM notebook.

Taking y as the wall-normal coordinate, we can decompose the velocity field into a mean and a perturbation, where the mean is averaged in x, z and t (under the assumption of a statistically steady state):

$$\boldsymbol{u} = \bar{\boldsymbol{u}}(y) + \boldsymbol{u}'(x, y, z, t), \quad \bar{\boldsymbol{u}} = (\bar{u}(y), 0, \bar{w}(y)), \quad \boldsymbol{u}' = (u', v', w'). \tag{C1a–c}$$

The (volume-averaged) kinetic energy can thus be decomposed into mean and turbulent components

$$\mathcal{K} \equiv \tfrac{1}{2}\langle|\boldsymbol{u}|^2\rangle = \tfrac{1}{2}(\langle\bar{u}^2 + \bar{w}^2\rangle + \langle|\boldsymbol{u}'|^2\rangle), \quad \bar{\mathcal{K}} \equiv \tfrac{1}{2}\langle\bar{u}^2 + \bar{w}^2\rangle, \quad \mathcal{K}' \equiv \tfrac{1}{2}\langle|\boldsymbol{u}'|^2\rangle. \tag{C2a–c}$$

From the momentum equation, we can then derive the budget equation for the total kinetic energy $\mathcal{K}$:

$$\underbrace{\frac{Uu_\tau^2}{H/2}}_{\mathcal{I}} + \underbrace{g\alpha\langle w\theta\rangle}_{q} = \underbrace{\nu\left\langle\frac{\partial u_i}{\partial x_j}\frac{\partial u_i}{\partial x_j}\right\rangle}_{\varepsilon}. \tag{C3}$$

Here, the energy input from the pressure gradient ($\mathcal{I}$) and the buoyancy flux (q) are balanced by viscous dissipation (ε).

Figure 17 presents how the relative importance of the two energy production terms changes as Re is increased. An excellent collapse is observed when the ratio $\mathcal{I}/q$ is plotted in terms of Re/Re_0, where $Re_0 = W_0H/\nu$ is defined (as earlier) using the peak

Gr	Pr	Re	$N_x = N_z$	N_y	N_x^r	N_y^r	C_f^u	Re_δ	C_f^w	Nu
10^6	1	3.16×10^2	512	192	1024	384	7.84×10^{-2}	36.8	1.66×10^{-1}	6.37
10^6	1	5.62×10^2	512	192	1024	384	4.46×10^{-2}	48.8	1.30×10^{-1}	5.98
10^6	1	1.00×10^3	512	192	1024	384	2.59×10^{-2}	61.1	1.00×10^{-1}	5.57
10^6	1	1.78×10^3	512	192	1024	384	1.57×10^{-2}	81.6	7.62×10^{-2}	5.33
10^6	1	3.16×10^3	768	192	1536	384	1.06×10^{-2}	85.2	6.89×10^{-2}	5.85
10^6	1	1.00×10^4	1024	192	2048	384	6.96×10^{-3}	43.2	1.91×10^{-1}	12.01
10^6	4	3.16×10^2	512	192	1024	384	7.27×10^{-2}	29.9	2.17×10^{-1}	9.39
10^6	4	5.62×10^2	512	192	1024	384	4.02×10^{-2}	41.3	1.60×10^{-1}	8.69
10^6	4	1.00×10^3	512	192	1024	384	2.30×10^{-2}	59.6	1.11×10^{-1}	8.15
10^6	4	1.78×10^3	512	192	1024	384	1.42×10^{-2}	74.6	8.74×10^{-2}	8.39
10^6	4	3.16×10^3	768	192	1536	384	1.01×10^{-2}	61.3	1.03×10^{-1}	10.46
10^6	10	3.16×10^2	512	192	1536	576	6.68×10^{-2}	28.7	2.43×10^{-1}	11.48
10^6	10	5.62×10^2	512	192	1536	576	3.64×10^{-2}	39.7	1.75×10^{-1}	10.73
10^6	10	1.00×10^3	512	192	1536	576	2.10×10^{-2}	58.2	1.22×10^{-1}	10.38
10^6	10	1.78×10^3	512	192	1536	576	1.33×10^{-2}	69.3	9.83×10^{-2}	11.16
10^6	10	3.16×10^3	768	192	2304	576	9.85×10^{-3}	45.3	1.53×10^{-1}	15.04
10^7	1	3.16×10^2	512	192	1024	384	1.44×10^{-1}	90.3	8.68×10^{-2}	13.74
10^7	1	1.00×10^3	512	192	1024	384	4.63×10^{-2}	99.8	7.46×10^{-2}	13.14
10^7	1	1.78×10^3	512	192	1024	384	2.72×10^{-2}	118.9	6.46×10^{-2}	12.47
10^7	1	3.16×10^3	768	192	1536	384	1.63×10^{-2}	136.7	5.31×10^{-2}	11.85
10^7	1	5.62×10^3	768	192	1536	384	1.04×10^{-2}	157.9	4.49×10^{-2}	12.06
10^7	1	1.00×10^4	1024	256	2048	512	7.52×10^{-3}	160.6	4.53×10^{-2}	14.39
10^8	1	1.00×10^3	1536	384	2304	512	8.71×10^{-2}	198.0	4.71×10^{-2}	28.14
10^8	1	3.16×10^3	1536	384	2304	512	2.90×10^{-2}	226.7	4.17×10^{-2}	27.05
10^8	1	1.00×10^4	1536	384	2304	512	1.07×10^{-2}	266.6	3.21×10^{-2}	25.82
10^6	1	0.00	512	192	1024	384	—	31.7	1.89×10^{-1}	6.62
10^6	4	0.00	512	192	1024	384	—	23.7	2.67×10^{-1}	10.09
10^6	10	0.00	512	192	1536	576	—	20.2	3.42×10^{-1}	12.76
10^7	1	0.00	512	192	1024	384	—	90.9	8.59×10^{-2}	13.76
10^8	1	0.00	1536	384	2304	576	—	181.3	4.97×10^{-2}	28.24

Table 1. Physical control parameters: Grashof number Gr, Prandtl number Pr, Reynolds number Re. Numerical grid parameters: number of grid points in the periodic (x, z) directions $N_x = N_z$ and wall-normal direction N_y for the base grid and for the refined grid ($N_x^r = N_z^r$ and N_y^r). Global response parameters: streamwise friction coefficient C_f^u, vertical boundary layer Reynolds number Re_δ, vertical friction coefficient C_f^w, Nusselt number Nu.

Name	Gr	Pr	Re	$N_x = N_z$	N_y	N_x^r	N_y^r	C_f^u	Re_δ	C_f^w	Nu
RB	10^7	1	0.00	2304	192	4608	384	—	45.0	1.65×10^{-1}	15.79
VC	10^7	1	0.00	2304	192	4608	384	—	89.9	8.74×10^{-2}	13.80
P-RB	10^7	1	3.16×10^3	2304	192	4608	384	1.47×10^{-2}	70.7	9.91×10^{-2}	12.01
P-VC	10^7	1	3.16×10^3	2304	192	4608	384	1.62×10^{-2}	134.1	5.45×10^{-2}	11.86

Table 2. Physical control parameters, numerical grid parameters and global response parameters for the extended domain simulations with $\Gamma = 24$ discussed in § 6. The statistics for these simulations were collected over only 100 advective time units due to the increased computational cost of the larger domains and the spectra calculations.

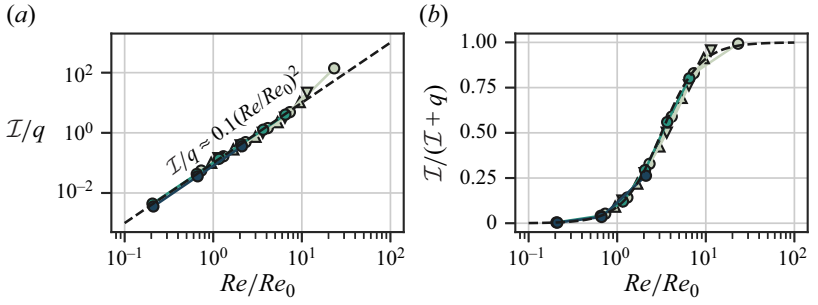

Figure 17. Components of the total kinetic energy budget in mixed VC. (*a*) Ratio of the energy input from the pressure gradient $\mathcal{I}$ to the energy input from the buoyancy q as a function of Re/Re_0. (*b*) Proportion of the total energy input produced by the pressure gradient. The dashed black line is an empirical fit to the data described by $\mathcal{I}/q = 0.1(Re/Re_0)^2$. Colours and symbols denote variation in Gr and Pr following the figures of § 4. This figure is also available as an interactive JFM notebook: https://www.cambridge.org/S0022112024005986/JFM-Notebooks/files/Figure-17.ipynb.

vertical velocity W_0 of the natural VC flow at matching Gr and Pr. An empirical estimate of $\mathcal{I}/q \approx 0.1(Re/Re_0)^2$ appears to describe the transition from buoyancy-dominant to pressure-dominant regimes, although there is currently no theoretical justification for this relationship. Although $\mathcal{I}$ can be related straightforwardly to the friction coefficient as $\mathcal{I} = C_f U^3/H$, there is no closed estimate for the vertical buoyancy flux q, even in natural VC.

In a similar manner as for the total kinetic energy, we can also derive a budget equation for the mean kinetic energy $\bar{\mathcal{K}}$ as

$$\underbrace{\frac{Uu_\tau^2}{H/2}}_{\mathcal{I}} + \underbrace{g\alpha\langle\bar{w}\bar{\theta}\rangle}_{\bar{q}} = \underbrace{\left\langle -\overline{v'\boldsymbol{u}'} \cdot \frac{\partial \bar{\boldsymbol{u}}}{\partial y}\right\rangle}_{\mathcal{P}} + \underbrace{\nu\left\langle \left|\frac{\partial \bar{\boldsymbol{u}}}{\partial y}\right|^2\right\rangle}_{\bar{\varepsilon}}, \tag{C4}$$

where the shear production $\mathcal{P}$ converts mean kinetic energy to TKE. Note that the two (horizontal and vertical) components of the mean kinetic energy can be completely decoupled, such that we can derive separate budgets for those quantities:

$$\underbrace{\frac{Uu_\tau^2}{H/2}}_{\mathcal{I}} = \underbrace{\left\langle -\overline{v'u'}\,\frac{\partial \bar{u}}{\partial y}\right\rangle}_{\mathcal{P}_u} + \underbrace{\nu\left\langle \left|\frac{\partial \bar{u}}{\partial y}\right|^2\right\rangle}_{\bar{\varepsilon}_u}, \quad \underbrace{g\alpha\langle\bar{w}\bar{\theta}\rangle}_{\bar{q}} = \underbrace{\left\langle -\overline{v'w'}\,\frac{\partial \bar{w}}{\partial y}\right\rangle}_{\mathcal{P}_w} + \underbrace{\nu\left\langle \left|\frac{\partial \bar{w}}{\partial y}\right|^2\right\rangle}_{\bar{\varepsilon}_w}. \tag{C5a,b}$$

The relative energy transfer in each of these budgets is shown in figure 18. For the horizontal component of mean kinetic energy presented in figures 18(*a*,*b*), we find that the proportion of energy transferred to TKE, $\mathcal{P}_u/\mathcal{I}$, is approximately constant at low Re for a given Gr, but increases at higher Re, with the trend suggesting independence of Gr at sufficiently high Re. This is reminiscent of the behaviour of C_f in figure 4, perhaps unsurprisingly since $C_f = \mathcal{I}/(U^3/H)$. Such a trend is not evident in the vertical component of the mean kinetic energy shown in figures 18(*c*,*d*). The vertical shear production $\mathcal{P}_w$ exhibits non-monotonic dependence on Re, and a reasonable collapse with Ri for the $Pr = 1$ data, but significant dependence on Pr otherwise. Larger Pr and lower Gr lead to a larger proportion of the energy supplied by the mean buoyancy flux $\bar{q}$ being directly dissipated by viscosity (through $\bar{\varepsilon}_w$).

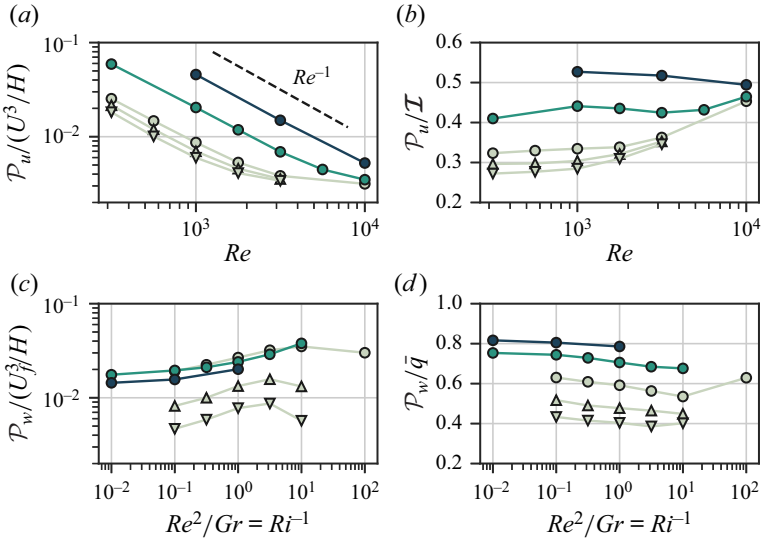

Figure 18. Budget contributions for the (*a*,*b*) horizontal and (*c*,*d*) vertical components of the mean kinetic energy. The horizontal component of shear production $\mathcal{P}_u$ is normalised by (*a*) the bulk velocity scaling U^3/H, and (*b*) the total energy injection due to the pressure gradient $\mathcal{I}$. The vertical component of shear production $\mathcal{P}_w$ is normalised by (*c*) the free-fall velocity scaling U_f^3/H, and (*d*) the buoyancy flux of the mean profiles $\tilde{q}$. This figure is also available as an interactive JFM notebook: https://www.cambridge.org/S0022112024005986/JFM-Notebooks/files/Figure-18.ipynb.

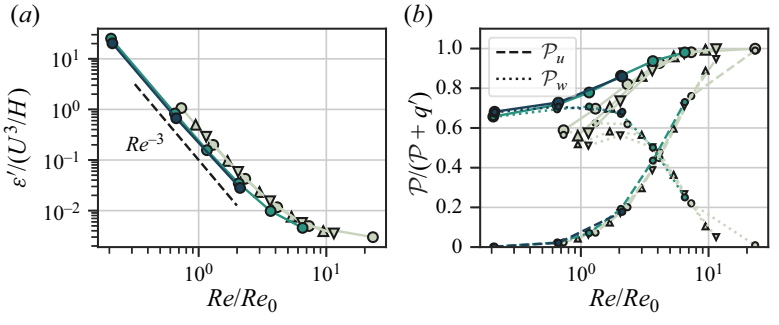

Figure 19. Budget contributions for the TKE. (*a*) TKE dissipation rate ε' normalised by U^3/H as a function of Re/Re_0. (*b*) Proportion of TKE produced by shear, decomposed into horizontal (dashed) and vertical (dotted) components. Symbols for the decomposed terms are made smaller than those for the total shear production. This figure is also available as an interactive JFM notebook: https://www.cambridge.org/S0022112024005986/JFM-Notebooks/files/Figure-19.ipynb.

Taking the difference of the total and mean kinetic energy budgets constructs the TKE budget for our system, which reads

$$\underbrace{-\overline{v'\boldsymbol{u}'}\,\frac{\partial \bar{\boldsymbol{u}}}{\partial y}}_{\mathcal{P}} + \underbrace{g\alpha\langle w'\theta'\rangle}_{q'} = \underbrace{\nu\left\langle \frac{\partial u_i'}{\partial x_j}\,\frac{\partial u_i'}{\partial x_j}\right\rangle}_{\varepsilon'}. \tag{C6}$$

Figure 19(*a*) shows that the TKE dissipation rate ε' data collapse as a function of Re/Re_0 when normalised by U^3/H. For $Re \leq Re_0$, a Re^{-3} scaling implies that ε' is independent

of U, whereas at higher Re/Re_0, the slope flattens out, potentially consistent with a finite value of dissipation as $Re \to \infty$. The remainder of the energy budget terms, shown in figure 19(*b*), also show a good collapse with Re/Re_0, highlighting the crossover from the natural convection limit where the vertical component of shear production $\mathcal{P}_w$ and the turbulent buoyancy flux q' balance the dissipation to the turbulent shear flow limit where the TKE production is dominated by the horizontal shear production $\mathcal{P}_u$. The collapse of the data in the transitional values of Re/Re_0 is somewhat surprising given that in the natural convection limit, the ratios of the budget terms varies significantly with Gr and Pr (Howland *et al.* 2022).

References

Alcántara-Ávila, F. & Hoyas, S. 2021 Direct numerical simulation of thermal channel flow for medium–high Prandtl numbers up to $Re_\tau = 2000$. *Intl J. Heat Mass Transfer* **176**, 121412.

Antonia, R.A., Abe, H. & Kawamura, H. 2009 Analogy between velocity and scalar fields in a turbulent channel flow. *J. Fluid Mech.* **628**, 241–268.

Blass, A., Tabak, P., Verzicco, R., Stevens, R.J.A.M. & Lohse, D. 2021 The effect of Prandtl number on turbulent sheared thermal convection. *J. Fluid Mech.* **910**, A37.

Blass, A., Zhu, X., Verzicco, R., Lohse, D. & Stevens, R.J.A.M. 2020 Flow organization and heat transfer in turbulent wall sheared thermal convection. *J. Fluid Mech.* **897**, A22.

Cheng, Y., Li, Q., Li, D. & Gentine, P. 2021 Logarithmic profile of temperature in sheared and unstably stratified atmospheric boundary layers. *Phys. Rev. Fluids* **6** (3), 034606.

Ching, E.S.C. 2023 Heat flux and wall shear stress in large-aspect-ratio turbulent vertical convection. *Phys. Rev. Fluids* **8** (2), L022601.

Couston, L.-A., Hester, E., Favier, B., Taylor, J.R., Holland, P.R. & Jenkins, A. 2021 Topography generation by melting and freezing in a turbulent shear flow. *J. Fluid Mech.* **911**, A44.

Daniels, K.E. & Bodenschatz, E. 2002 Defect turbulence in inclined layer convection. *Phys. Rev. Lett.* **88** (3), 034501.

Domaradzki, J.A. & Metcalfe, R.W. 1988 Direct numerical simulations of the effects of shear on turbulent Rayleigh–Bénard convection. *J. Fluid Mech.* **193**, 499–531.

El-Samni, O.A., Yoon, H.S. & Chun, H.H. 2005 Direct numerical simulation of turbulent flow in a vertical channel with buoyancy orthogonal to mean flow. *Intl J. Heat Mass Transfer* **48** (7), 1267–1282.

Foken, T. 2006 50 years of the Monin–Obukhov similarity theory. *Boundary-Layer Meteorol.* **119** (3), 431–447.

Gage, K.S. & Reid, W.H. 1968 The stability of thermally stratified plane Poiseuille flow. *J. Fluid Mech.* **33** (1), 21–32.

Grossmann, S. & Lohse, D. 2000 Scaling in thermal convection: a unifying theory. *J. Fluid Mech.* **407**, 27–56.

Grossmann, S. & Lohse, D. 2001 Thermal convection for large Prandtl numbers. *Phys. Rev. Lett.* **86** (15), 3316–3319.

Guo, W. & Prasser, H.-M. 2022 Direct numerical simulation of turbulent heat transfer in liquid metals in buoyancy-affected vertical channel. *Intl J. Heat Mass Transfer* **194**, 123013.

Howland, C.J., Ng, C.S., Verzicco, R. & Lohse, D. 2022 Boundary layers in turbulent vertical convection at high Prandtl number. *J. Fluid Mech.* **930**, A32.

Howland, C.J., Verzicco, R. & Lohse, D. 2023 Double-diffusive transport in multicomponent vertical convection. *Phys. Rev. Fluids* **8** (1), 013501.

Jackson, R.H., Nash, J.D., Kienholz, C., Sutherland, D.A., Amundson, J.M., Motyka, R.J., Winters, D., Skyllingstad, E. & Pettit, E.C. 2020 Meltwater intrusions reveal mechanisms for rapid submarine melt at a tidewater glacier. *Geophys. Res. Lett.* **47** (2), e2019GL085335.

Kader, B.A. & Yaglom, A.M. 1972 Heat and mass transfer laws for fully turbulent wall flows. *Intl J. Heat Mass Transfer* **15** (12), 2329–2351.

Kader, B.A. & Yaglom, A.M. 1990 Mean fields and fluctuation moments in unstably stratified turbulent boundary layers. *J. Fluid Mech.* **212**, 637–662.

Kasagi, N. & Nishimura, M. 1997 Direct numerical simulation of combined forced and natural turbulent convection in a vertical plane channel. *Intl J. Heat Fluid Flow* **18** (1), 88–99.

Kays, W.M., Crawford, M.E., Weigand, B. & Kays, W.M. 2005 *Convective Heat and Mass Transfer*, 4th edn. McGraw-Hill Higher Education.

KE, J., WILLIAMSON, N., ARMFIELD, S.W. & KOMIYA, A. 2023 The turbulence development of a vertical natural convection boundary layer. *J. Fluid Mech.* **964**, A24.

KLINE, S.J., REYNOLDS, W.C., SCHRAUB, F.A. & RUNSTADLER, P.W. 1967 The structure of turbulent boundary layers. *J. Fluid Mech.* **30** (4), 741–773.

KRUG, D., LOHSE, D. & STEVENS, R.J.A.M. 2020 Coherence of temperature and velocity superstructures in turbulent Rayleigh–Bénard flow. *J. Fluid Mech.* **887**, A2.

LEE, M. & MOSER, R.D. 2015 Direct numerical simulation of turbulent channel flow up to $Re_\tau \approx 5200$. *J. Fluid Mech.* **774**, 395–415.

LI, M., JIA, P., LIU, H., JIAO, Z. & ZHANG, Y. 2023 Mean velocity and temperature profiles in turbulent vertical convection. *J. Fluid Mech.* **977**, A51.

LOHSE, D. & SHISHKINA, O. 2023 Ultimate turbulent thermal convection. *Phys. Today* **76** (11), 26–32.

MADHUSUDANAN, A., ILLINGWORTH, S.J., MARUSIC, I. & CHUNG, D. 2022 Navier–Stokes-based linear model for unstably stratified turbulent channel flows. *Phys. Rev. Fluids* **7** (4), 044601.

MONIN, A.S. & OBUKHOV, A.M. 1954 Basic laws of turbulent mixing in the surface layer of the atmosphere. *Tr. Geofiz Inst. SSSR* **24** (151), 163–187.

MONKEWITZ, P.A. & NAGIB, H.M. 2023 The hunt for the Kármán 'constant' revisited. *J. Fluid Mech.* **967**, A15.

NG, C.S., OOI, A., LOHSE, D. & CHUNG, D. 2015 Vertical natural convection: application of the unifying theory of thermal convection. *J. Fluid Mech.* **764**, 349–361.

OBUKHOV, A.M. 1946 Turbulence in an atmosphere with a non-uniform temperature. *Boundary-Layer Meteorol.* **1**, 95–115.

ORLANDI, P., BERNARDINI, M. & PIROZZOLI, S. 2015 Poiseuille and Couette flows in the transitional and fully turbulent regime. *J. Fluid Mech.* **770**, 424–441.

OSTILLA-MONICO, R., YANG, Y., VAN DER POEL, E.P., LOHSE, D. & VERZICCO, R. 2015 A multiple-resolution strategy for direct numerical simulation of scalar turbulence. *J. Comput. Phys.* **301**, 308–321.

PALLARES, J., VERNET, A., FERRE, J.A. & GRAU, F.X. 2010 Turbulent large-scale structures in natural convection vertical channel flow. *Intl J. Heat Mass Transfer* **53** (19), 4168–4175.

PIROZZOLI, S., BERNARDINI, M. & ORLANDI, P. 2014 Turbulence statistics in Couette flow at high Reynolds number. *J. Fluid Mech.* **758**, 327–343.

PIROZZOLI, S., BERNARDINI, M., VERZICCO, R. & ORLANDI, P. 2017 Mixed convection in turbulent channels with unstable stratification. *J. Fluid Mech.* **821**, 482–516.

PIROZZOLI, S. & ORLANDI, P. 2021 Natural grid stretching for DNS of wall-bounded flows. *J. Comput. Phys.* **439**, 110408.

VAN DER POEL, E.P., OSTILLA-MÓNICO, R., DONNERS, J. & VERZICCO, R. 2015 A pencil distributed finite difference code for strongly turbulent wall-bounded flows. *Comput. Fluids* **116**, 10–16.

PRANDTL, L. 1932 Zur turbulenten Strömung in Rohren und längs Platten. In *Ergebnisse der aerodynamischen Versuchsanstalt zu Göttingen* (ed. L. Prandtl & A. Betz), vol. 4, pp. 18–29. Oldenbourg Wissenschaftsverlag.

QUADRIO, M., FROHNAPFEL, B. & HASEGAWA, Y. 2016 Does the choice of the forcing term affect flow statistics in DNS of turbulent channel flow? *Eur. J. Mech.* B*/Fluids* **55**, 286–293.

RAVICHANDRAN, S., TOPPALADODDI, S. & WETTLAUFER, J.S. 2022 The combined effects of buoyancy, rotation, and shear on phase boundary evolution. *J. Fluid Mech.* **941**, A39.

RICHTER, F.M. & PARSONS, B. 1975 On the interaction of two scales of convection in the mantle. *J. Geophys. Res.* **80** (17), 2529–2541.

SCAGLIARINI, A., EINARSSON, H., GYLFASON, Á. & TOSCHI, F. 2015 Law of the wall in an unstably stratified turbulent channel flow. *J. Fluid Mech.* **781**, R5.

SCAGLIARINI, A., GYLFASON, Á. & TOSCHI, F. 2014 Heat-flux scaling in turbulent Rayleigh–Bénard convection with an imposed longitudinal wind. *Phys. Rev.* E **89** (4), 043012.

SCHLICHTING, H. & GERSTEN, K. 2016 *Boundary-Layer Theory*, 9th edn. Springer.

VERZICCO, R. & ORLANDI, P. 1996 A finite-difference scheme for three-dimensional incompressible flows in cylindrical coordinates. *J. Comput. Phys.* **123** (2), 402–414.

WELLS, A.J. 2023 From classical to ultimate heat fluxes for convection at a vertical wall. *J. Fluid Mech.* **970**, F1.

WETZEL, T. & WAGNER, C. 2019 Buoyancy-induced effects on large-scale motions in differentially heated vertical channel flows studied in direct numerical simulations. *Intl J. Heat Fluid Flow* **75**, 14–26.

YERRAGOLAM, G.S., HOWLAND, C.J., STEVENS, R.J.A.M., VERZICCO, R., SHISHKINA, O. & Lohse, D. 2024 Scaling relations for heat and momentum transport in sheared Rayleigh–Bénard convection. *J. Fluid Mech.* (submitted). arXiv:2403.04418.

YERRAGOLAM, G.S., VERZICCO, R., LOHSE, D. & STEVENS, R.J.A.M. 2022 How small-scale flow structures affect the heat transport in sheared thermal convection. *J. Fluid Mech.* **944**, A1.

ZHENG, Z., HARCOURT, R.R. & D'ASARO, E.A. 2021 Evaluating Monin–Obukhov scaling in the unstable oceanic surface layer. *J. Phys. Oceanogr.* **51** (3), 911–930.